MICROCOPY RESOLUTION TEST CHART

NATIONAL BUREAU OF STANDARDS-1963-A
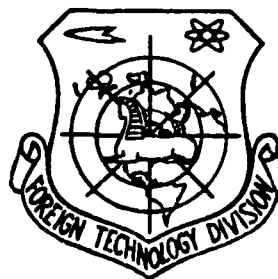
ADA140181

FOREIGN TECHNOLOGY DIVISION

JOURNAL OF AERONAUTICAL MATERIALS

(Selected Articles)

DTIC
SELECTED
APR 17 1984
B

DTIC FILE COPY

84 04 16 155

EDITED TRANSLATION

FTD-ID(RS)T-1870-83   27 March 1984

MICROFICHE NR: FTD-84-C-000315

JOURNAL OF AERONAUTICAL MATERIALS (Selected Articles)

English pages: 119

Source: Hangkong Cailiao, Vol. 3, Nr. 1, 1983, pp. 1-7;
         8-12; 17-22; 23-29; 30-35; 36-40; 41-45; 53-58;
         11 unnr

Country of origin: China
Translated by: LEO KANNER ASSOCIATES
               F33657-81-D-0264
Requester: FTD/TQTA
Approved for public release; distribution unlimited.

GRAPHICS DISCLAIMER

All figures, graphics, tables, equations, etc. merged into this
translation were extracted from the best quality copy available.

i

TABLE OF CONTENTS

INFLUENCES OF REMNANT DENDRITE ON THE SERVICE PROPERTIES FOR THE TURBINE DISK OF GH36 ALLOY

Zhou Ruifa

Abstract

This paper studies the influences of tensile strength, impact ductility, rupture life, high and low cycle fatigue life and fracture toughness for the turbine disk of GH36 alloy. It gives the relationship between the low cycle fatigue fracture life (N_f) and the steady tensile stress (σ_{st}) when there is remnant dendrite as:

$$\lg N_f = a + b \lg \sigma_{st}, \qquad b < 0$$

Test results show that remnant dendrite noticeably decreased the fracture toughness value for the turbine disk of GH36 alloy. In this paper, the Paris formula was used to calculate critical crack length (a_c) in accordance with the equivalent stresses σ_{eq} and Kl_c of the turbine disk.

In this paper, we also discuss the influences of several factors such as the cooling rate of ingot and the forging ratio. We also brough forth the proposal of the quality control standard for the turbine disk of GH36 alloy.

I. Preface

The turbine disk is an important heat component of the gas turbine engine. Under high speed rotation and gas corrosion conditions, each component sustains different temperatures and stress: the temperature of the wheelboss is low and its stress is large; during repeated starting and stopping cycles, the rim has high temperature, the cycle stress value of the centrifugal force and thermal stress superposition is large and sometimes

1

the stress of the mortise tooth slot bottom etc. sections approaches or surpasses the yield stress. Therefore, the requirements for material strength and its homogeneity are very high.

Remnant dendrite, carbide segregation and large crystalline grains are the three main material quality problems often seen on turbine disks of GH36 alloy [1]. This type of situation is also widely existent on turbine disks of other alloys. Because of this, in research, the influences of the problems of material on service safety and life, which are the influences on the various mechanical properties as well as the investigation of its formation causes and improvement measures, have universal significance.

This paper selected the influences of remnant dendrite on the properties of turbine disks of GH36 alloy as the research content and the aim is to find the key techniques and standards for improving material homogeneity and to investigate the influences of increasing the forging ratio on material homogeneity. The critical crack length, after using fracture mechanics to discuss materials showing cracks, acts as a reference for future production and outside service maintenance.

II. Test Method

The composition (%) of the turbine disk of GH36 alloy used for research is: CO.36;SiO.60;Mn8.50;Cr12.63;Ni8.6;Mo1.23;V1.37; Nb0.60; Fe is the remainder. It was made from 10 ton arc furnace smelting, 2.6 ton octagonal ingot going through forging press cogging and die forging. The samples used for measuring properties were cut along the tangent of the turbine disk. In order to study the influences of remnant dendrite on the different places of the turbine disk during use, we comprehensively determined the tensile, impact, rupture, bending and axial low

2

cycle fatigue, fracture toughness etc. mechanical properties.

The low cycle fatigue selected equisectional smooth samples with controlled axial strain and the tests were carried out in strain ratio R=-1, triangular waves, frequency f=3 times/minute and the controlled total strain range was 0.4-1%. The heat treatment system used for the samples was: 1140°C/3 hours, water cool; then in 670°C/16-18 hours raise to 780°C/18-20 hours, air cool. The electronic probe was used for contrastive analysis of dendritic axis and interdendritic chemical composition.

III. Test Results

3.1 Influences of Remnant Dendrite Structure on Mechanical Properties

(1) The Influences on Room Temperature Properties. These are shown in Table 1. The remnant dendrite structure did not decrease the tensile strength of alloys, the percentage elongation (δ) and sectional shrinkage rate (ψ) had certain decreases slightly lower than the technical condition requirements and the alloy's impact value (a_k) had marked decreases, the lowest decreasing to $0.75 kg \cdot m/cm^2$.

(1) 试验项目	(6) 室温性能					650°C 32kg/mm²			650.C 35kg/mm²			650°C 38kg/mm²		
	σ_b	$\sigma_{0.2}$	δ	ψ	a_k	τ (7)	δ	ψ	τ (8)	δ	ψ	τ (9)	δ	ψ
(3)	kg/mm²		%		kg·m/cm²	时:分	分	%	时:分		%	时:分		%
(2) 残留枝晶 无 (3)	92.5	—	22.0	35.0	3.8,4,4.3	442:45	2.8	4.3	264:25	2.0	1.8	111:30	4.0	4.1
(2) 组织 有 (4)	92.5	—	15.8	15.9	0.75,0.75	5?3:54	2.4	3.9	247:15	2.4	3.9	92:50	2.0	4.3
(5) 技术条件	85	80	15	20	2.5	—	—	—	100	—	—	35	—	—

Table 1 Influences of remnant dendrite structure on properties.
Key: (1) Test item; (2) Remnant dendrite structures; (3) Without; (4) With; (5) Technical conditions; (6) Temperature properties; (7)-(9) Time: minutes.

3

(2) The Influences on 650°C Rupture Properties. As shown in Table 1, the results of tests done at 650°C under different stress conditions show that under effects of static load, remnant dendrite does not have marked influences on the rupture strength and plasticity of alloys.

(3) The Influences on Bending Fatigue Properties. As shown in Table 2, because of the existence of remnant dendrite struct- ures, the bending fatigue properties of GR36 alloy markedly decreased. The forging press deformation of the turbine disk's rim is large and the casted dendrite structure was completely crushed; the wheelboss deformation is small, the casted remnant dendrite structure was relatively serious and the fatigue pro- perties markedly decreased. It is one reason for the production of fatigue property fluctuations for the turbine disk of GH36 alloy. The results of comparisons are shown in Fig. 1. The instability of the forging press technique is the determining factor. The bending fatigue properties directly influence the safety and life of the mortise teeth. For samples without rem- nant dendrite structure, $48kg/mm^2$ fatigue life can reach 10^7 cycles. On the contrary, for samples with serious remnant dendrite structure, at 600°C, the $42kg/mm^2$ fatigue life is only 3.6×10^4 cycles. It causes the fatigue limit to fluctuate and decrease $6-8kg/mm^2$.

σ, kg/mm²	40	42	44	46	48	50	52
(1) 有残留枝晶 N_f, 次	1.27×10⁷ >1×10⁷	>1.03×10⁷ 3.6×10⁴	>1.14×10⁷ >1.15×10⁷	2.37×10⁴ 2.53×10⁴ <1.3×10⁴	—	—	1.1×10⁴ 1.15×10⁴
(2) 无残留枝晶 N_f, 次	—	—	—	1.77×10⁶ >1.3×10⁷	>1×10⁷	3.8×10⁴	1.8×10⁴

Table 2 Influences of remnant dendrite structure on 600°C bending fatigue.
Key: (1) With remnant dendrite N_f, times; (2) Without remnant dendrite N_f times.
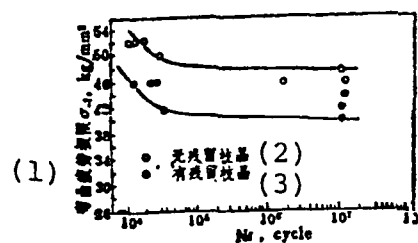
4

Fig. 1 Comparison of fatigue properties with and without remnant dendrite.

Key: (1) Bending fatigue limit, (2) Without remnant dendrite; (3) With remnant dendrite.

(4) The Influences on High Temperature Low Cycle Fatigue Properties. As shown in Table 3, at 300 and 600°C, the total strain range is $\pm 0.4\sim1.0\%$, strain ratio R=-1 and frequency f=3 times/minute. The test results of fatigue cycle stability stress and fracture cycle life are shown in Fig. 2.

(1) 试验温度 °C	±0.4%		±0.6%		±0.8%		±1.0%	
	σ_{st}	N_f,次 (2)	σ_{st}	N_f,次 (3)	σ_{st}	N_f,次 (4)	σ_{st}	N_f,次 (5)
300	46	11571	58.6	1759	62.6	705	65.7	504
	46.7	6673	60.0	1191	65.2	548	63.5	779
600	40.5	3267	54.1	129	55.2	103	56.7	70
	44.7	1028	61	202	59.0	115	55.3	344

(6) 注: σ_{st}一稳定应力=½$\Delta\sigma_{st}$（稳定应力范围之半）, kg/mm^2

Table 3 Influences of samples with remnant dendrite structure on low cycle fatigue.

Key: (1) Test temperature; (2)-(5) Times; (6) Note; σ_{st} is the steady stress=1/2 Δ σ_{st} (half of steady stress range).
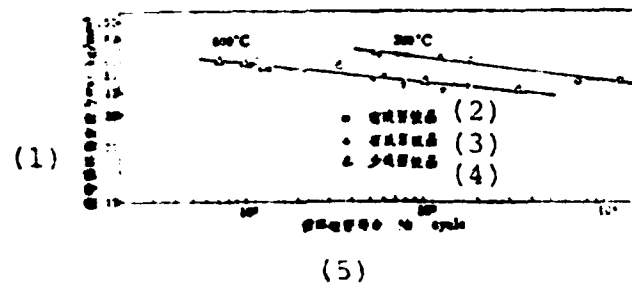
5

(5)

Fig. 2 Influences of remnant dendrite on turbine disks of
GH36 alloy on low cycle fatigue life.

Key: (1) Fatigue cycle steady stress; (2) Without
remnant dendr.   (3) With remnant dendrite; (4)
Little remnant dentrite; (5) Cycle fatigue life.

Test results show that when there is remnant dendrite struct-
ure on the turbine disk of GH36 alloy and it is at 300°C, there
is still relatively high low cycle fatigue life. When the total
strain is ±0.4%, the fracture cycle life reaches 6,678 times;
when the remnant dendrite is light it can reach 11,571 times.
However, there is marked decrease at 600°C and there are only
1,028 times when the total strain is ±0.4%. Fracture observa-
tions prove that when samples have relatively serious remnant
dendrite and short lives, this is one major reason for low cycle
fatigue life fluctuation. Therefore, when operating at 600°C,
it is necessary for the structures of the rim section to carry
out stringent control. After the low cycle fatigue data of 300
and 600°C goes through regression analysis, they are separately
expressed as follows:

$$300℃: \lg N_f = 17.52176 - 8.12920 \sigma_s. \quad (1)(可信度99\%)$$
$$600℃: \lg N_f = 18.38803 - 9.23717 \sigma_{st} \quad (2)(可信度98\%)$$

Key: (1)-(2) Believability.

In the formula, the constant (sectional distance) and coefficient
(slope) in front of steady tensite stress σ_{st} are constants
which change with the test temperature and material (including

6

the remnant dendrite structure). The remnant dendrite structure causes the above mentioned constant and coefficient to decrease and thus decrease the low cycle fatigue life.

(5) The Influences on Fracture Toughness. The fracture toughness samples are cut on the turbine disk and we selected relatively thin samples to carry out the tests. We used the J integration method to measure K_{Ic}, that is

$$J_{Ic} = \frac{2U}{B(W-a)} \qquad \text{(1)}\qquad 则 \qquad K_{Ic} = \sqrt{J_{Ic}\,\frac{E}{1-v^2}}$$

Key: (1) Then.

In the formulas, U is the strain energy; B is the sample's thickness; W is the height of the sample; a is the crack length; E is the elastic modulus; v is the Poisson ratio.

As shown in Table 4, the remnant dendrite in the center of the disk is more serious than on the rim and its K_{Ic} value is much lower, the lowest being 224kg/mm$^{3/2}$.

(1) 组织状态	B	W	a	W-a	J_{Ic} kg/mm	K_{Ic} kg/mm$^{3/2}$
(2) 有残留枝晶 （轮心）	25.3	19.2	19.2	9.01	2.2	224
	20.14	30.18	17.44	12.74	2.6	244
(3) 无残留枝晶 （轮缘）	20.10	30.12	17.50	12.60	4.4	316
	20.26	30.24	17.36	12.86	4.8	331
	20.32	30.26	17.38	12.80	5.2	343

Table 4 Influences of remnant dendrite strucures on K_{Ic}.
Key: (1) Structural state; (2) Without remnant dendrite (wheelboss); (3) Without remnant dendrite (rim).

3.2 Remnant Dendrite Structure Analysis and Fracture Observations.

7

Table 5 shows the electronic probe analysis. The composition of the dendrite axle and that of the alloy are the same; there are large amounts of Nb and V carbides within the dendrite and also a type of high chromium phase. In this, the oxides of the Nb and V assume a fish bone shape; the high chromium phase assumes a block shape. After forging press machining, they all assume zonal distribution and crush with the increase of the deformation level.

(1) 分析元素	Fe	Cr	Ni	Mn	Nb	V	Mo
(2) 枝晶轴（基体）	45.70	14.44	8.0	10.0	0.058	2.60	0.85
枝晶间（碳化物）	—	—	—	—	19.40	79.84	—
(3) （高铬相）	21.15	46.0	1.40	5.94	1.70	23.40	5.10

Table 5   Probe analysis results (%) of the compositions of different locations of remnant dendrite.

Key: (1) Analyzed element; (2) Dendrite axle (base body); (3) Within the dendrite (oxides), (high chromium phase).

Fracture analysis shows that: as shown by the bending fatigue cracks in Fig. 3 (see Plate 1), there are high chromium phase and niobium and vanadium carbide cracks begin and propagate along the remnant dendrite; as shown by the low cycle fatigue cracks in Fig. 4 (see Plate 1), the fracture surface is parallel to the direction of the high chromium phase and carbide distribution within the dendrite which in the same way proves the phase beginning and propagation along the dendrite; the metal phase structure in the fracture area of the fracture toughness sample are seen in Fig. 5 (see Plate 2) and its remnant dendrite structure with low fracture toughness is relatively serious as shown in Fig. 5a. When the scanning microscope was used to observe the fractures of low cycle fatigue samples, it was discovered that the fatigue cracks propagated along the carbide and remnant

8

dendrite concentrated area. See Fig. 6 (see Plate 2).

IV. Discussion of Problems

4.1 Formation, Control and Improved Path of Dendrite

The ingot casted crystals are divided into the fine crystal, columnar crystal and isometric crystal areas. The crystals all accorded with the patterns of the larger the dendrite and steel ingot the greater the interdendritic distance; the higher the melting rate the greater the interdendritic distance [2]. By raising the solidification rate, we can cause the dendrite to branch, decrease the dendritic cells, the distance between the branches and trunk as well as the dimensions of the interisometric second phase [3]. In the solidification process, there is the following relationship between solidification index η, and temperature gradient G and solidification speed R [4]:

$$\eta = GR^{-1}$$

Between dendritic cell dimension y and solidification rate X, there exists the following relationship:

$$y = AX^{-1/3}, \text{ A is the material's constant}$$

Between interdendritic distance d and cooling rate V, there is a linear relationship on the double logarithm coordinate [5,6], that is

$$d = AV^{-b}, \text{ b is the cooling speed index}$$

Naturally, decreasing the interdendritic distance is directly related to decreasing the segregation dimensions and this can only be realized by increasing the cooling rate. If we use electroslag or vacuum self-consuming remelting, because the water cooled crystal causes the interdendritic distance to decrease, it correspondingly causes the inclusions and second phase carbide dimensions to also decrease. This has very good effects on

9

raising the standard of material and service properties and lowering property fluctuations. Naturally, enlargement of the forging ratio is also a method of improving the dendritic defects. This will be discussed below.

4.2 Influences of Remnant Dendrite Structures on the Use of Turbine Disks

We separately carry out discussion based on the different utilization places of the turbine disk:

(1) The turbine disk's wheelboss sustains the largest tensile stress but the stress amplitude is not large. A certain machine's equivalent stress $\sigma_{eq}=54.3kg/mm^2$; Table 4 gives the K_{Ic} with and without remnant dendrite structure as 224 and $343kg/mm^{3/2}$; if the turbine disk has central surface cracks, because the radius of the crack dimensions facing the disk is very small, we use the expression of infinite surface crack K_I [7], that is

$$K_I = \sqrt{1.21\pi a} \; \sigma / \sqrt{Q}$$

When K_I is the K_{Ic}, then a is critical crack a_c, that is

$$a_c = \frac{K_{Ic}^2}{1.21\pi\sigma^2} Q = \frac{K_{Ic}^2}{1.21\pi\sigma_{ec}^2} Q$$

As shown in Fig. 7, if a/2c=0.2 and $\sigma_{eq}/\sigma_{0.2}=54.3/52=1.05$, calculated according to $Q = \phi^2 - 0.212(\sigma/\sigma_{0.2})$ or by referring to the tab le, we can obtain the crack's geometric strength factor Q value as 1.05. We substitute the above data into a_o formula and the calculated results are as listed in Table 6.
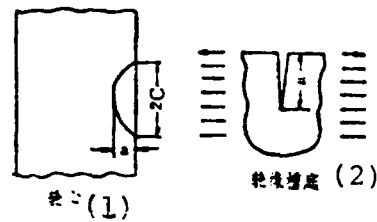
10

Fig. 7 Simplified mechanical calculation model chart of cracks
of turbine disk's wheelboss and rim positions.

Key: (1) Wheelboss; (2) Rim's slot bottom.

(1) 受力部位	(4) 组织状态 (5)	K_{1c}	σ	$\sigma_{0.2}$,*	a_c,
		$kg/mm^{3/2}$	kg/mm^2		mm
(2) 轮盘中心	有残留枝晶	224	54.3	52	4.7
	无 (6)	343	54.3	52	11.0
(3) 轮缘槽底	有 (7)	224	47	49	5.7
	无 (8)	343	47	49	13.3

(9) *考虑受力部位温度影响的应力值。

Table 6 Influences of remnant dendrite on critical crack
length a_c.

Key: (1) Stress position; (2) Disk center; (3) Rim
slot base; (4) Structure state; (5) With remnant
dendrite; (6) Without; (7) With; (8) Without;
(9)*Considering the stress value of the stress
position's temperature influence.

(2)   When the rim of the turbine disk sustains cycle fatigue
stress and the stress amplitude is large, the slot bottom and
tightly sealed tooth cracks can appear and it is necessary that
the low cycle fatigue properties be good. When the low cycle
fatigue properties of GH36 alloy are low, especially under the
effects of salt spray and gas corrosion, the slot bottom can
have cracks within 100 hours. Therefore, it is necessary to
discuss the critical crack length a_c value when there is a
remnant dendrite structure. We can do comparative calculations

11

based on the expression given in Reference [8], that is

$$a = \frac{1}{(1.13)^2 \pi} \left(\frac{K_{1c}}{\sigma} \right)^2$$

Assuming a certain machine's slot bottom cracks simplified mechanical calculation model as shown in Fig. 7, the tangential stress of the slot bottom's crack position is $47 kg/mm^2$ and when we substitute in the above formula the calculation results are as listed in Table 6. The influences of the remnant dendrite on the residual life can be calculated based on a_o and cycle stress range $\Delta\sigma$, that is

$$N_p = \frac{a_c^{1-\frac{n}{2}} - a_i^{1-\frac{n}{2}}}{C\left(1-\frac{n}{2}\right)\left[1.3 \Delta\sigma\pi^{\frac{1}{2}}\right]^n}$$

$$n \neq 2$$

In the formula, c and n are obtained from crack propagation tests and they are influenced by stress, frequency, structure, environment and other factors.

(3) The mortise teeth of the turbine disk sustain somewhat lower stress amplitude than the slot bottom. Because they are affected by the starting and stopping centrifugal force bending moment, they are also affected by the superposition of the blade 's high frequency vibratory stress. Mortise teeth cracks are one of the commonly seen breakdowns and the breakdown fracure characteristics are very similar to those of bending fatigue fractures. The bending fatigue data can be used as the criterion for the ser   roperties of mortise teeth. It was proven from bending f   ts that because the turbine disk of GH35 alloy has ı   endrite, the fluctuation of the bending fatigue limit is large . The fluctuation range is from 40-48 kg/mm^2 which has marked influence on the service safety and life of the mortise teeth. After the mortise teeth have cracks, because the fracture toughness of the remnant dendrite is low

12

and the dimensions of the mortise teeth are thin, it is relatively easy to lose teeth and thus create breakdowns.

To sum up, because the influence of remnant dendrite structure on wheelboss strength such as σ_b and $\sigma_{0.2}$ is not great, when there are no cracks we can allow them to exist to a small extent; because the rim clearly produces fatigue property fluctuation and decrease it should be stipulated that it is not permissable for a remnant dendrite structure to exist which can be seen with the naked eye.

4.3 Influences and Control of the Forging Ratio

The selected crystals, segregation and non-uniform structure often produced during the ingot casting process can cause the properties to be non-uniform and especially lower fatigue properties and fracture toughness. The casting process in essence, is one technical means to improve and eliminate structural and property non-uniformity. Systematic tests of the forging ratio of 40CrNiMoA steel show that when the forging ratio increased its properties improved. For example, the fatigue limit in the forged state was 37kg/mm^2; when the forging ratio was 1-4 it was 49kg/mm^2; when the forging ratio was 4-6 it was 50-51kg/mm^2; when the forging ratio was 6-8 it could steadily reach 53-54 kg/mm^2; there was no noticeably influence upon further increasing the forging ratio. As shown in Fig. 8, in 13% Cr steel [9], the room temperature and 400°C fatigue limit σ_{-1} rose with the increase of the forging ratio. When the forging ratio was between 0-10, σ_{-1} had a sudden change area and it was necessary for the forging ratio to be larger than 6 to be able to avoid this fluctuation area and be larger than 10 to enter the stable area.
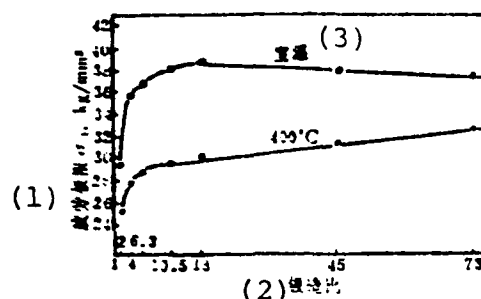
13

Fig. 8   Influence of forging ratio on fatigue limit of Cr steel.
Key: (1) Fatigue limit; (2) Forging ratio; (3) Room
temperature.

The forging ratio of the wheelboss of the turbine disk of
GH36 alloy is small, the remnant dendrite structure is relatively
serious and the non-uniform structure causes the properties to
decrease and fluctuate. By increasing the forging ratio, we
can cause interdendritic high chromium phase and carbide crush-
ing and diffused distribution. By controlling the forging
ratio, we cause it to avoid the sudden change area below 6 and
it is required to reach 8. This causes the alloy to enter the
structurally and property stable area. This is totally neces-
sary for the turbine disk rim and it satisfies the predeter-
mined condition of the standard requirement for the rim not to
allow a dendrite (cast state) structure to be visible to the
naked eye.

V.   Conclusion

1.   The remnant dendrite structure on the turbine disk of
GH36 alloy is formed when the cast ingot is influenced by the
cooling rate during the solidification process and the forging
ratio is insufficient. The interdendritic high chromium and
niobium and vanadium carbides exist by means of the separation
state.

14

2.   Research shows that the remnant dendrite structure of GH36 alloy on the turbine disk cause the tensile plasticity and impact ductility to decrease; the bending fatigue and low cycle fatigue properties to have relatively large fluctuations and decreases; it clearly decreases fracture toughness; but does not lower the tensile and rupture strength.

3.   Fracture analysis shows that the high chromium phase and carbide separation within the remnant dendrite is a direct cause of plasticity, impact, fatigue and fracture toughness decreases.

4.   The remnant dendrite structure causes the fracture toughness of turbine disks of GH36 alloy to decrease from 343 to $224kg/mm^{3/2}$. We simultaneously used the Paris and K_I equations, substituted in the rim's tangential stress value and checking the computation and by contrasting the slot bottom's critical crack length a_c value we showed that rims with and without remnant dendrite structures have marked influences on the residual life.

I recommend that the engine's turbine disk standard should be revised and add the clause that "the rim section does not allow remnant dendrite and carbide etc. separation which can be seen by the naked eye to exist." It guarantees the quality and life of the turbine disk as well as the limiting clause of the forging press technique etc. I consider that the standard photograph (Fig. 9, see Plate 2) of the original machine's remnant dendrite structure of GH36 alloy is only applicable for the quality requirements of this machine's control amplitude plate section and is not applicable in the rim section.

References

[1] Zhou Ruifa, Journal of Aeronautical Materials, 1(1981), No. 1,1.

[2] Deries, R.P. and Muman, G.R., J. of Metals,(1968), No. 33.

[3] Spear, R.E. and Gardner, G.R., Modern Castings, 31(1960)No.1.

[4] Berry, J.T., Trans. AFS, 78(1970), 421.

[5] Flemings, M.G., Metal Technology, 6(1979), No.2.

[6] Morris Cohon, "The Evolution and Prospects of Materials Science and Engineering", May, 1980 lecture in Beijing.

[7] Lai Zuhan, Foreign Aviation, 5(1975), 19.

[8] NASA. TND-7483.

[9] Shoya Sasako, Iron and Steel, 43(1957), 537.

16

Fig. 3 Bending fatigue fracturing along remnant dendrite, 600°C, 42kg/mm^2, N_f=3.67x10^4 times.

17
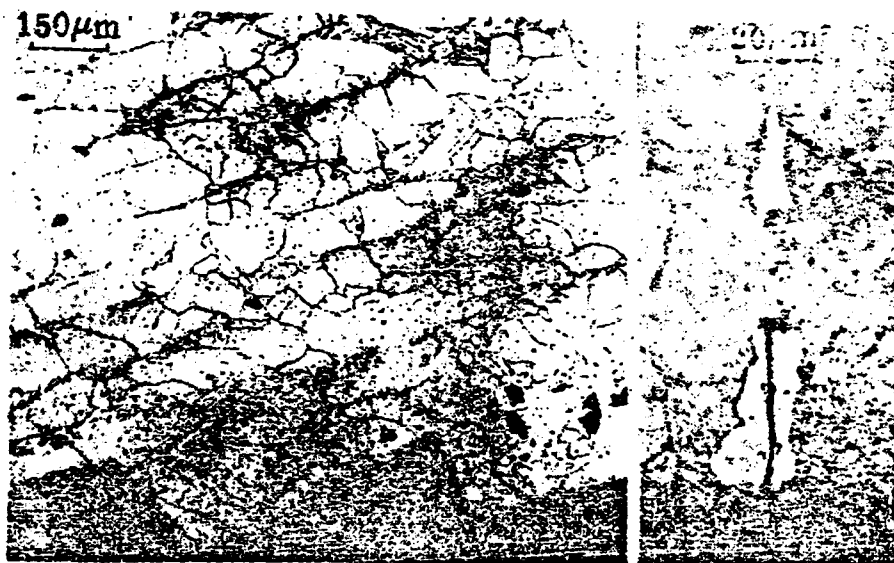
Fig. 4   Low cycle fatigue cracking fracturing along remnant dendrite, 600°C, 55.2kg/mm^2, N_f=100 times ($\Delta \mathcal{E}_r$=$\pm$0.8%).
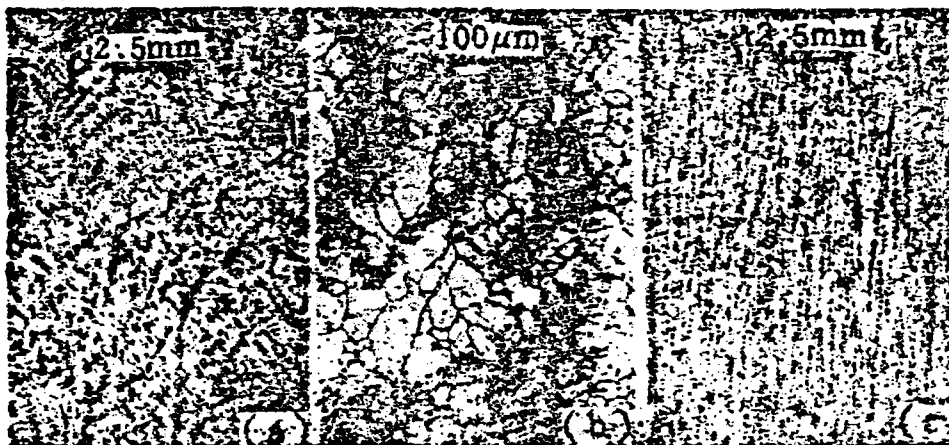
Fig. 5 Relationship of fracture toughness (K_{1c}) and remant dendrite.

Key: (a) K_{1c}=224kg/mm$^{3/2}$, remant dendrite serious; (b) Same as a; (c) K_{1c}=343kg/mm$^{3/2}$, remnant dendrite forge crushing.

Fig. 6 Observation results of low cycle fatigue cracking along carbide and remnant dendrite using scanning electron microscope, 600°C, 54.1kg/mm^2, N_f=129 times.

19

Fig. 9   Allowable level of remnant dendrite structure (standard
         piece photograph), (applicable for amplitude plate, it
         is a bearing ring control standard photograph).

STUDY OF THE SUPERPLASTICITY OF Ti 679 ALLOY

Yang Zhenheng, Su Zuwu, Zhou Yigang and Chen Shisun
(Northwestern Polytechnical University)
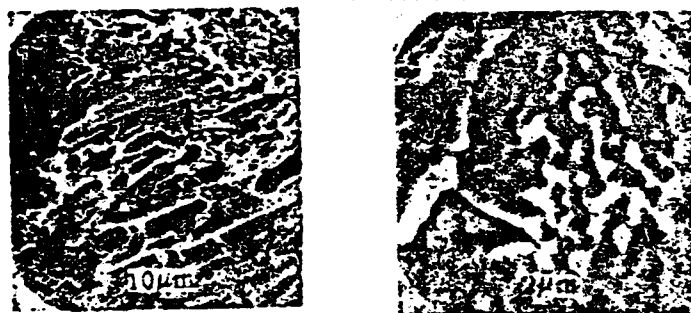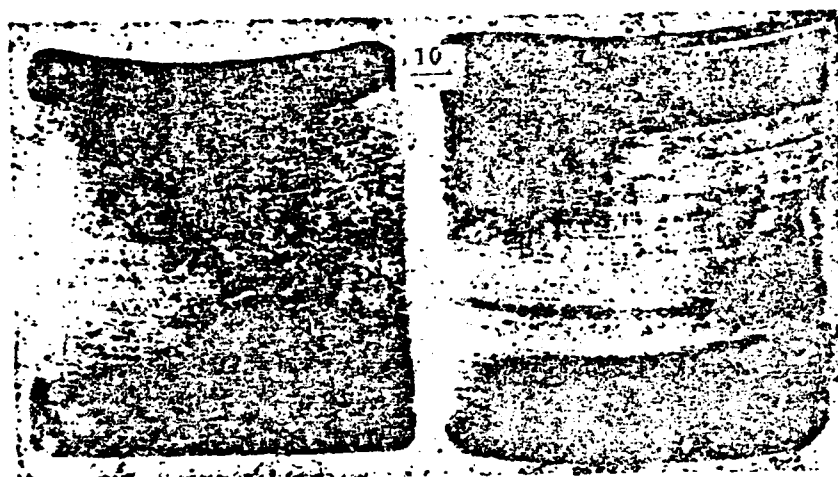
Abstract

This paper studies the superplastical forming conditions of
Ti 679 alloy. We carried out tensile tests on a high temperature
tester, measured the sensitivity index m value of stress on the
strain rate and also studied the metallographic structures in
different states.

Test results showed that there is superplasticity in the
720-900°C temperature range and the m values are all above 0.3.
800-850°C is the plasticity high value range and 850°C is taken
as the optimal superplasticity range. Under this temperature,
when the strain rate is 6.67×10^{-4} seconds^{-1}, the elongation is
734% and the corresponding m value is 0.43.

In this paper, we collated the deformation temperature,
speed, elongation, deformation resistance and other relational
curves of Ti 679 alloy which can provide reference for determin-
ing the technical specifications when there is superplastical
forming.

I. Preface

Ti 679 alloy is a near α type high temperature titanium
alloy which is mainly used to make the compressors, sealed coils
and blade etc. forgings of Spay turbofan engines. Because this
type of alloy has excellent combined service properties, it has
also been used in other industries.

This paper used tensile tests to measure the sensitivity
index m value of the stress of Ti 679 alloy in a superfine crystal

21

state on the strain rate as well as the elongation (δ) under different temperatures and determined the pattern of the m value and δ value changing with the deformation temperature and strain rate. Thus, we found that the superplastical temperature and speed conditions of this alloy provide correct technical parameters for superplastical deformation.

II. Test Method

The tests used the rolled rod produced by the Fushun Steel Mill as the raw material. Its chemical composition (%) is: 2.5Al, 11.02Sn, 5.2Zr, 0.97Mo, 0.24Si, 0.14Fe, 0.021C, 0.072O_2, 0.0058H_2, 0.026N_2 and the remainder is Ti.

In order to obtain a superfine crystal structure, a ϕ22mm rolled rod underwent two firings at 900°C on a 250 kilogram air hammer and was forged into a ϕ15mm rod. The deformation level was 53.7% and it was air cooled after forging. Afterwards, it was annealed for 1 hour in an 800°C resistance furnace, air cooled and after testing, the size of the α phase was 2.02 micron. The ϕ15 rod forging machine machined a standard tensile sample with a ϕ5x25mm standard length.

The tensile tests and determination of the m value were all carried out on the Daojin IS-10T variable speed high temperature tension tester. The control temperature error of the electric furnace on the tester did not exceed ±2°C and the samples all began tensile elongation after maintaining the temperature for 20 minutes at the test temperature.

We used the sudden speed change method to determine the m value and Fig. 1 is a model chart of this method.
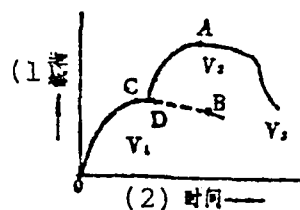
Fig. 1   Chart of using the sudden speed change method to deter-
         mine the load-tine relation of the m value.

         Key: (1) Load; (2) Time.

We first used V_1 velocity tensile elongation and after the load
was stable we quickly approximately doubled the tensile elonga-
tion velocity to V_2 and continued the elongation. The C point
is the maximum load point under V_1 velocity, A is the maximum
load point at V_2 velocity and we extrapolated the load-time
curve at V_1 velocity to the B point so that the absolute elonga-
tion of the B point and the absolute elongation of the A r-int
at V_2 velocity were equal. We measured the load at the A and
B points as P_A and P_B and then the m value was found by the
following formula:

$$m = \lg \frac{P_A}{P_B} \Big/ \lg \frac{V_2}{V_1}$$

III.   Test Results and Analysis

3.1   The m Value

When there is superplastical deformation, following the in-
crease of the strain rate, the sensitivity index of the
rheological stress on the strain rate is indicated by the m
value. Figure 2 shows the relationship of the m value measured
from Ti 679 alloy at 800°C and the strain rate. When the strain
rate is 1.67×10^{-4} seconds^{-1}, the maximum m value is 0.44 and
when the strain rate decreases or increases, the m value always

23

lowers. When there is a low strain rate, diffusion creeping is the main mechanism of deformation. Under low velocity, the deformation time is long and the crystal grain grows a little. When there is a high strain rate, the climbing of dislocations occupies a dominant position, grain boundary behavior decreases and the change law of the m value is related to this.

3.2 The Optimal Superplastical Temperature

The Ti679 alloy test rod used 1mm/minute velocity tensile elongation (strain rate $\mathcal{E} = 6.67 \times 10^{-4}$ seconds^{-1}), the test temperatures were 720, 760, 780, 800, 850, 870 and 900°C and the obtained elongation and temperature relational curve is as shown in Fig. 3. The m value in relative temperature is as shown in the figure. We can see from the figure that at 850°C, the elongation is maximum and when three test rods have tensile elongation the elongation of one among them reaches 734% but it still does not break. We can see from the changes of the m value curve that at 850°C the corresponding m=0.43 is also the maximum value. It can be seen that the optimal superplastical temperature strain of this alloy is 850°C. This is different from the superplastical temperature of Ti 679 alloy being 800°C and the corresponding elongation of 500% mentioned in Reference [2].
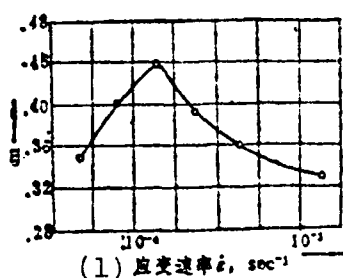

(1) 应变速率 $\dot{\varepsilon}$, sec^{-1}

Fig. 2 Relationship of m value and strain rate at 800°C.
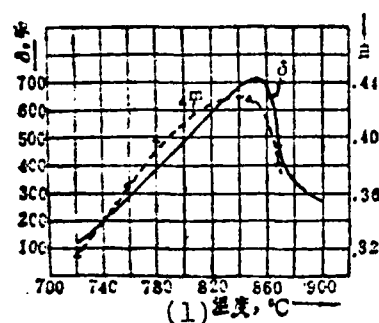   Key: (1) Strain rate.

24

Fig. 3   Relationship of the δ and m values and the deformation temperature.

Key: (1) Temperature.

Further, we can see from Fig. 3 that in the 720-900°C temperature range, the alloy always has superplasticity, the δ value is in the 126-734% range and the m values are all larger than 0.3. Therefore, it can be considered that the Ti679 alloy possesses a relatively wide superplastical temperature range. If this type of alloy is used for superplastical forming, based on the different deformation levels required by the forging and the existing equipment tonnage, we can separately select different superplastical temperatures.

Figure 4 (see Plate 3) is a photo of an object after tensile elongation. As regards the surface state of the sample after analyzing the tensile elongation, for samples with elongation above 850°C, surface oxidation is relatively noticeable but this phenomenon does not exist below 800°C and the surface is smooth. We can see from this that if this type of alloy has superplastical forming at 800°C, we will be able to obtain a forging with a surface of excellent quality. If we use 850°C superplastical forming, then we should adopt protective measures such as spraying glass lubricant etc.

3.3   The Optimal Strain Rate

Figure 5 shows the relationship of the m values and

25

temperatures of Ti (?)9 alloy under different strain rates. When the strain rate is 6.67×10^{-5} seconds^{-1}, the temperature corresponding to the maximum m value is 850 °C;

when the strain rate is 1.67×10^{-4} sec^{-1} the temperature corresponding to the maximum m value is 800°C

is 1.67×10^{-3} seconds^{-1}, the maximum m value then corresponds to 820°C. Therefore, within the three above mentioned strain rate ranges, the m values which correspond to 800-850°C are always maximum. If we use an m value larger than 0.3 as the index to determine the alloy's superplasticity, then in the above mentioned strain rate ranges, it should always be considered that the alloy has superplasticity in the 780-850°C range.
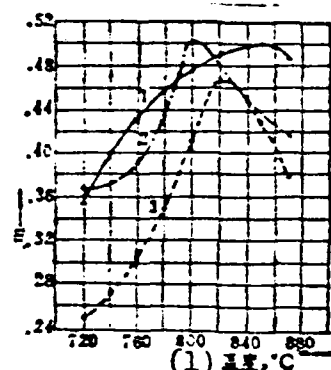
图 5 不同应变速率下的m值和温度的关系

(2)

1、$V_1 = 0.1 \dfrac{mm}{min}$ $\dot{\varepsilon}_1 = 6.67 \times 10^{-5}$秒$^{-1}$

2、$V_2 = 0.25$ $\dot{\varepsilon}_2 = 1.67 \times 10^{-4}$

3、$V_3 = 2.5$ $\dot{\varepsilon}_3 = 1.67 \times 10^{-3}$

Fig. 5 Relationship of m values and temperatures under different strain rates.

Key: (1) Temperature; (2) Seconds.

Figure 6 shows the changes of the m and δ values with the strain rate at 850°C. We can see from the figure that when the strain rate is smaller than 6.67×10^{-3} seconds^{-1}, the corresponding m value is larger than 0.3 and the δ value is larger

than 270%. Therefore, it can be considered that if the Ti 679 alloy carries out superplastical forming at 850°C, we should select a strain rate smaller than 6.67×10^{-3} seconds^{-1}. Moreover, we take the strain rate equal to 6.67×10^{-4} seconds^{-1} (the corresponding tensile rate is 1mm/minute) as optimum. The corresponding m value (m=0.43) and δ value (δ=734%) are maximum at this strain rate.

(1) 应变速率ε̇, sec⁻¹
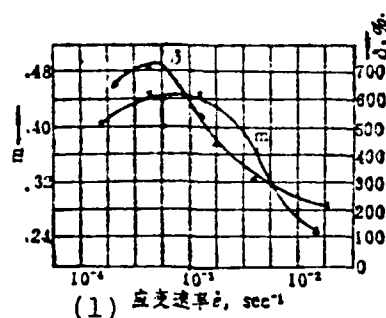
Fig. 6   Situation of the m and δ values changing with the strain rate at 850°C.

Key: (1) Strain rate.

3.4   Deformation Resistance

See Fig. 7 for the pattern of the real stress of Ti 679 alloy which changes with the tensile temperature and tensile velocity. In the figure, the change pattern of the curve shows the real stress of the alloy which decreases with the rises of the deformation temperature and decreases of the deformation velocity. Under the above mentioned optimal superplastical temperature (850-800°C) and superplastical deformation velocity, the real deformation resistance of the alloy is very small, σ =3.15-7.03kg/mm^2. In the figure, the provided data can act as reference for determining the deformation resistance value when there is superplastical forming.

Fig. 7   Relationship of the real stress and deformation temper-
ature and the deformation velocity.

Key: (1) Temperature.

3.5   High Power Structure of the Alloy Before and After
Deformation

Figure 8 (see Plate 3) shows the high power structure of the
Ti 679 alloy ϕ 22mm roll rod.   After being determined by the
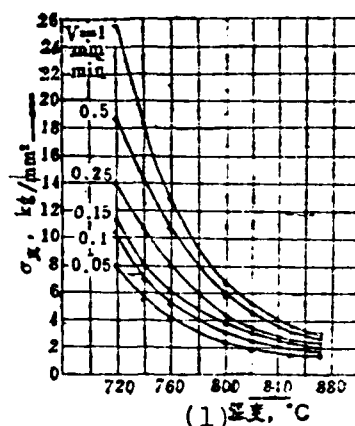picture analyzer, initial α occupied 16% of the total area of
the field of vision and Weishi(?) α occupied 14.78%.

After forging the ϕ 22mm rolled rod into a ϕ 15mm rod, it
then went through 800°C or 900°C annealing for 1 hour and after
cooling its metallographic structures are separately shown in
Figs. 9a and b (see Plate 3).   The initial α size in Fig. 9a
measured by the picture analyzer calculated according to the
chord length is 2.02μm, the initial α and Weishi(?)α occupy
47% of the total area of the visual field and the visible
crystal grains were made finer.   In order for the superplastical
deformation to provide structural conditions, when the α and β
phase contents were close, it was advantageous to inhibit the
growth of the grain when stopped for a long time at high tem-
perature so as to guarantee steady superplastical forming.

28

The α content and morphology shown in Figs. 9a and b are slightly different. Because the temperature of the latter is relatively high, α is completely dissolved, residual α becomes even finer and smaller, the material with this type of structure which is shown in Fig. 9b is machined into a test rod and we carry out tests at 850°C using 1mm/minute elongation velocity. The measured elongation is 614.5% and when compared with the elongation of 734% obtained from the corresponding test sample with high power structure shown in Fig. 9a, the difference is not great. Therefore, use of the annealing system with 800 or 900°C maintained temperature for 1 hour and air cooling has no great effects on the plasticity of the alloy.

Figures 10a, b and c (see Plate 3) are separately high power structures of test samples after 800, 850 and 900°C tensile fractures. By comparing them with Figs. 9a, we can see that although the samples after 800°C tensile elongation underwent tensile deformation for a long period of time, during the elongation process, the size of the grain basically remained unchanged and was still very fine. After 850° tensile elongation, the grain size of the sample grew larger as compared to before tensile elongation yet still maintained a certain level of fineness. Therefore, the alloy always has relatively high plasticity at 800 and 850°C but the grain size of the sample after 900°C tensile elongation markedly grows and elongation δ markedly decreases (δ =270°). This is naturally due to the influences of high temperature.

When considering the structural morphology of the alloy, at 800°C superplastical forming is more advantageous than at 850°C.

IV. Conclusion

1. Chinese-made Ti 679 alloy is an excellent type of superplastical alloy and in the 780~850°C temperature range, there

is plasticity when the strain rate is lower than 6.67×10^{-3} seconds^{-1}. Based on the requirements for the formation of different forgings, we can select corresponding temperatures and velocities.

2. The optimal superplastical temperature of Ti 679 alloy is 850°C and the optimal strain rate is 6.67×10^{-4} seconds^{-1}. Under these conditions, the elongation of the alloy can reach to over 734% and the sensitivity index of the stress to the strain rate is m=0.43. Yet, due to the tensile elongated sample's grain becoming coarse at 850°C, the surface quality is not good (oxidation is noticeable). If superplastical forming changes to use 800°C, then this drawback will not exist yet plastic index δ value will be slightly lower.

3. When the strain rate is 6.67×10^{-4} seconds^{-1}, the real stress of 800°C superplastic deformation is 7kg/mm^2 but the real stress at 850°C is only 3.2kg/mm^2.

4. The Ti 679 alloy rolled rod undergoes 57% deformation level reforging and after the annealing treatment of maintaining the temperature at 800°C for 1 hour and cooling, we will obtain an isometric superfine crystalline structure, the α size is 2.02μ m and the α phase occupies 47% of the total area of the visual field for the superplastical deformation to create structural conditions. After reforging, the forged rod maintains temperature at 900°C for 1 hour, goes through a cooling process, the contents of the α phase decrease and the residual α becomes even finer and smaller yet the influence on the δ value is not great.

Wang Chengping of the Northwestern Polytechnical University and Lin Rongsen, Zhou Qiheng, Wan Baoxiang et al of the Hongyuan Casting and Forging Factory also participated in the research work for this paper and we received a great deal of support and

help from the Metallographic Room of the Hongqi Machine Factory.
We would like to express our gratitude to them here.

References

[1] Bakofen, W.A., Turner, I.R. and Avery, D.H., Trans. ASM
    Quart 57, 1964, 980.

[2] Progress in Materials Science, 21(1976), No.2.
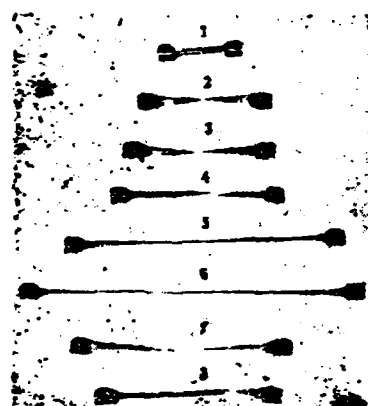
(1) 1—原始试样；
(2) 2—720°C拉后，δ=126%；
(3) 3—760°C拉后，δ=165%；
(4) 4—780°C拉后，δ=258%；
(5) 5—800°C拉后，δ=550%，未断；(9)
(6) 6—850°C拉后，δ=734%，未断；(10)
(7) 7—870°C拉后，δ=370%；
(8) 8—900°C拉后，δ=270%

Fig. 4 Photograph of a sample after tensile elongation tests.

Key: (1)Original sample; (2)~(8) After tension;
(9)-(10) Not yet fractured.

Fig. 8 Metallographic structure of raw material.

Fig. 9 Metallographic structures of forged rods after annealing.

Key: (a) 800°C annealing; (b) 900°C annealing.
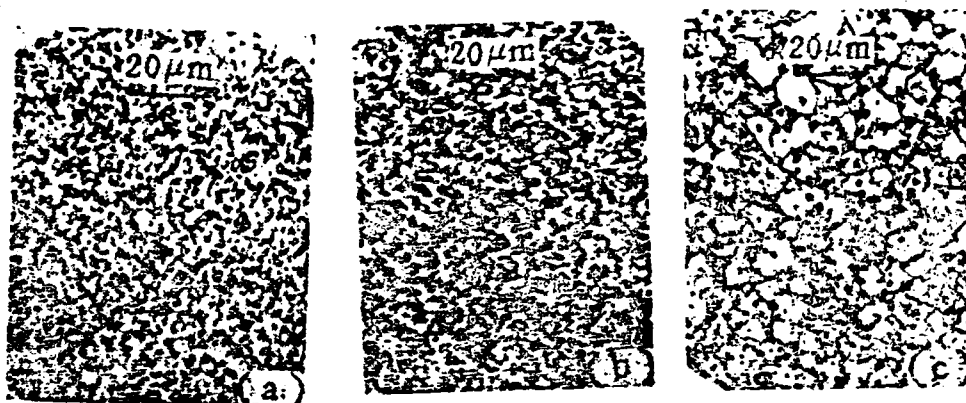
Fig. 10   Metallographic structures of test rod after tensile
          elongation.

          (a) 800°C tensile elongation; (b) 850°C tensile elongation;
          (c) 900°C tensile elongation.

EXPERIMENTAL RESEARCH ON SILICON CARBIDE FIBER REINFORCED ALUMINUM COMPOSITES

Wei Ketai, Huang Dadun and Zhao Xun
(Changsha Institute of Technology)

Abstract

This paper is an experimental research report on aluminum composites reinforced with silicon carbide fiber. We used continuous silicon carbide fiber and Chinese-made aluminum foil as the raw materials and used pressing liquid-infiltration in vacuum to make a composite plate. The fibers were not seriously damaged, the distribution was relatively uniform and the quality and performance were relatively good. The longitudinal tensile strength of part of the sample reached the ROM value and the transverse strength was higher than the calculated value. We discussed the relationship between the strength of the composite and the volume fraction of the fiber. We determined the volume fraction of the fiber, carried out analysis of the fracture morphology with a scanning microscope and a metallographic analysis of the transverse tensile samples and also briefly discussed the problem of interface strength.

I. Preface

The continuous development of aeronautical and aerospace engineering technology has brought higher and higher demands on material performance. As regards structural materials, the main demands are strength, specific strength, modulus and high specific modulus. Its aim is to decrease structural weight, increase the effective load and enlarge the range. In order to meet the demands of this type of daily increasing development, over the last 10 or 20 years, while researching how to improve the performance of commonly used materials, people have made inroads in the development work of composites. Here, we will mainly

deal with metal base composites. Among metal base composites, fiber reinforced metal occupies the most important position. The fiber reinforced metal composites which have been studied more often domestically and abroad are boron fiber, carbon fiber, aluminum oxide fiber, silicon carbide fiber reinforced aluminum, magnesium, titanium, nickel and their alloys. For example, the AVCO Company of the United States began development work on continuous silicon carbide fiber reinforced aluminum made by the chemical gas phase sedimentation method. The Materials Laboratory of the United States Air Force studied silicon carbide whisker reinforced aluminum. Japan is now developing the continuous silicon carbide fiber reinforced aluminum, magnesium, titanium, nickel etc. invented by Shito Kaishi. There are also some domestic schools and institutes which are doing development work in carbon fiber, boron fiber and silicon carbide fiber reinforced aluminum.

Internationally, boron fiber reinforced aluminum composites were used in aerospace and aircraft structures between 1975 and 1978. In the last one or two years, other fiber reinforced metal composites have been in the experimental research stage. Domestically, the above mentioned fiber reinforced metal composites are all being experimentally researched and there is still a distance before they can be applied in engineering. Given this situation, we developed experimental research work on continuous silicon carbide fiber reinforced aluminum composites and in the last two years we have attained preliminary results. We will now present a brief summary of them.

II. Test Materials

2.1 Silicon Carbide Fiber

Among the metal base composites, there are four forms of silicon carbide fiber which are used as reinforcing agents. Their major properties are given in Table 1.

35

(1)纤维种类	(5)纤维形式	直径 (10)10μ	比重 g/cm³ (11)	抗拉强度 kg/mm² (12)	弹性模量 kg/mm² (13)	(14)备注
Nicalon	(6连续束丝 (400~500根)	10~15	2.55	200~250	1.5×10⁴	(1)
(2)钨芯SiC	(7连续单丝	100~150	4.09	315		(2)
(3)碳芯SiC	(8连续单丝	100~150	4.09	350		(3)
(4)SiC晶须(9)不连续单丝		1~5	3.18	840~1050		(4)

Table 1   Properties of various silicon carbide fibers.

    Key: (1) Fiber type; (2) Tungsten core; (3) Carbon core; (4) Whisker; (5) Fiber form; (6) Continuous bound wire (400-500 wires); (7) Continuous single wire; (8) Continuous single wire; (9) Non-continuous single wire; (10) Diameter; (11) Specific weight; (12) Tensile strength; (13) Elastic modulus; (14) Remarks.

The SiC fiber which we used was Nicalon produced by the Nippon Carbon Company.

2.2   Base Metal

We used the Chinese-made industrially pure aluminum (LIM) as the metal base of the composite. There were several types with thicknesses of 0.03, 0.05, 0.3 and 0.5mm, the specific gravity was $2.77g/cm^3$, the strength was $5-10kg/mm^2$ and modulus $E \approx 7600kg/mm^2$.

III.   Composite Method

3.1   Selection of Composite Method

There are varied methods for making fiber reinforced metal composites. When selecting the composite method, we must consider: whether or not the base body can fully "infiltrate" the "space" between the fibers; whether or not the fiber distribution reaches uniformity; whether or not the interface joining

between the fiber and base body is good, that is, whether or not the interface can have relatively good shearing strength and tensile strength, there is no damage to the fiber during the composite process (such as breaking, crushing etc.); the cost and other factors.

Based on the special characteristics of using fiber bound wires we considered the above factors and referred to Reference [4] which was published abroad. After experimental investigations, we decided to use the pressing liquid-infiltration in vacuum method to make the plate sample of silicon carbide fiber reinforced aluminum composite.

3.2 Pressing Liquid-Infiltration in Vacuum

The process of this method can be divided into the following five steps:

(1) Arrangement and Seal Welding. Beforehand, we arrange it so that after the SiC fiber has no latitude zone and the aluminum foil is cut into certain dimensions, it is alternately arranged in a stainless steel mold case and afterwards we use argon arc welding to carry out sealing and to check leaking (see Fig. 1a).

(2) Degluing. We evacuate the stainless steel mold case equipped with SiC fiber and aluminum foil (vacuity is 10^{-1} -10^{-2}mmHg) and afterwards place it in a muffle furnace and heat to 400-450°C. Stopping for 30~40 minutes, we can then remove the organic glue applied on the SiC fiber surface (see Fig. 1b).

(3) Melting. After degluing, raise the temperature to 720°C and keep it there for 10 minutes. The aluminum then melts into a liquid. The vacuity should be above $10^{-1}-10^{-2}$mmHg (see Fig. 1c).

(4) Pressing Infiltration. After melting, we take the mold case out of the furnace and quickly place it on the press to be

37

immediately pressed so that the aluminum liquid infiltrates between the fibers causing the fiber distribution to be uniform and to attain very good interface joining (see Fig. 1d).

(5) Removing the Mold. After eliminating the pressed flat stainless steel mold case, we then obtain the plate sample of silicon carbide fiber single direction reinforced aluminum composite (see Fig. 1e).
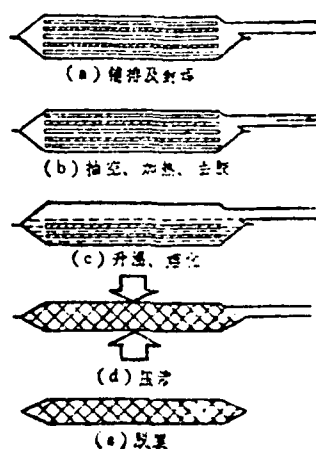
Fig. 1 Schematic of pressing liquid infiltration in vacuum process.

Key: (a) Arrangement and seal welding; (b) Evacuation, heating and degluing; (c) Raise temperature, melting; (d) Pressing infiltration; (e) Removing the mold.

IV. Tensile Test

4.1 Tensile Test Piece

The tensile test piece is shown in Fig. 2. The silicon carbide in the silicon carbide reinforced aluminum composite is too hard and the aluminum is too soft. The tools are very easily worn dull during the machining process and thus sample

38

machining is a troublesome problem. A more ideal method is to carry out machining by using a molybdenum wire cutter. This type of machining method can attain samples with relatively accurate dimensions and relatively good smooth finish.

Fig. 2 The tensile test piece.

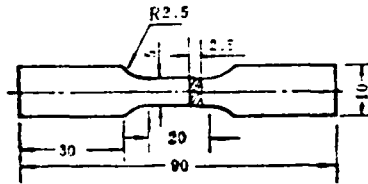4.2 The tensile test piece is divided into two types. One is longitudinal wherein the fiber and load directions are the same. The other is transverse wherein the fiber is perpendicular to the tensile load direction.

The tensile test was carried out on a Chinese-made BL-1000B electronic tension tester. The tensile velocity was 2mm/S. See Tables 2 and 3 for the test results.

(1) 试样号及数量	(2) 纤维体积分数 V_f, V/0	(3) 纵向拉伸强度 $\sigma_{c.l}$		(6) 断口特征
		(4) 实验值	(5) ROM值*	
L_{1-4}	10	8.3~14.0	24.5	斜断口 (7)
L_{2-1}	10	12.3	24.5	斜断口 (8)
L_{3-2}	15	18.8~30.4	34.2	平直断口 (9)
L_{4-4}	16	25.8~36.6	36.2	杯状断口 (10)
L_{5-4}	16.5	36.6~43.0	37.2	杯状断口 (11)
L_{6-1}	20	20.0	44.0	平直断口 (12)
L_{7-2}	20	28.0~31.0	44.0	平直断口 (13)
L_{8-4}	24.2	16.3~213	52.8	平直断口 (14)
L_{9-4}	25	27.5~30.9	53.7	平直断口 (15)
L_{10-4}	29.5	50.6~61.0	60.3	杯状断口 (16)
L_{11-2}	35	25.1~29.3	73.2	平直断口 (17)
L_{12-3}	40	46.5~50.9	83.0	斜断口 (18)

(19)*ROM为混合物定则（Rule of Mixture）的缩写，ROM值即理论计算值。

Table 2　Longitudinal tensile strength (kg/mm^2).

Key: (1) Sample number and quantity; (2) Volume fraction of fiber; (3) Longitudinal tensile strength; (4) Test value; (5) ROM value; (6) Fracture characteristics; (7)-(8) Oblique fracture; (9) Flat fracture; (10)-(11) Cup fracture; (12-(15) Flat fracture; (16) Cup fracture; (17) Flat fracture; (18) Oblique fracture; (19)*ROM is an abbreviation for Rule of Mixture and the ROM value is the theoretical calculated value.

(1) 试件号及数量	(2) 纤维体积分数 V_f, V/0	(3) 横向拉伸强度 $\sigma_{c.t}$		断口特征
		(4) 实验值	(5) 理论值[8]	(6)
T_{1-4}	11.0	8.3	4.22~3.24	斜断口 (7)
T_{2-4}	24.0	—	3.93~2.31	平直断口 (8)
T_{3-4}	32.0	9.0	3.83~1.87	杯状断口 (9)
T_{4-2}	46.0	13.4	3.72~1.21	杯状断口 (10)
T_{5-4}	0	5.2	—	—

Table 3　Transverse tensile　strength (kg/mm^2) (see next page).

Table 3 (continued)

Key: (1) Test piece number and quantity; (2) Volume
fraction of fiber; (3) Transverse tensile strength;
(4) Test value; (5) Theoretical value[5];
(6) Fracture characteristics; (7) Oblique fracture;
(8) Flat fracture; (9)-(10) Cup fracture.

V. Metallography and Fracture Analysis

5.1 Determination of Volume Fraction of Fiber

The volume fraction which the fiber occupies in the composite
directly influences the performance of the composite. Therefore,
determination of the volume fraction of the fiber (V_1,V/0) has
important significance. We used the quantitative metallographic
method to measure the volume fraction of silicon carbide fiber.
Figure 3 (see Plate 7) shows the metallographic photographs of
composites with different volume fractions.

5.2 Analysis of Fracture Morphology

The fracture characteristics and fracture morphology of
composite tensile test pieces can reflect the level of the com-
posite's strength as well as the quality of the composite. The
fractures of the L3, L6, L8, L9, L11 etc. test pieces have flat
characteristics. Analysis of the fracture morphology with a
scanning microscope (Fig. 4, see Plate 7) shows that the com-
posite quality of this type of sample is relatively poor. Either
the fiber has serious lamination (Fig. 4a), the damage to the
fiber is serious (Fig. 4b), the fiber distribution is not
uniform or the base body has looseness (Fig. 4c). However, the
fractures of the L5, L10 etc. test pieces have cup characteristics
and analysis of the fracture morphology shows that the quality
of these types of samples is relatively good. The fiber has
uniform distribution, does not have serious damage and has normal
fiber pulling out phenomena (Figs. 5a and b, see Plate 8).

5.3 Metallographic Analysis of Transverse Tensile Test
Pieces

41

The transversely cut sample was abraded and polished on one side and afterwards there was tensile fracturing on the tester. Figure 6 (see Plate 8) shows the metallographic photos and scanning microscope photos during the tensile fracturing process and after the tensile fracturing. They show that the transverse fractures of the composite occurred on the base body and interface.

VI. Discussion

6.1 Longitudinal Strength

The longitudinal strength of fiber single directional reinforced metal composites can be measured by the ROM value. The composite rule's strength formula is:

$$\sigma_{cul} = \sigma_{fu}V_f + (\sigma_m)\,\varepsilon'_f\,(1-V_f)$$

In the formula, σ_{cul} is the longitudinal tensile strength of the composite; σ_f and V_f separately indicate the tensile strength and volume fraction of the fiber; $(\sigma_m)_{\varepsilon'_f}$ is the strain of the composite which is equal to the stress of the base body metal when the fiber has fracture strain.
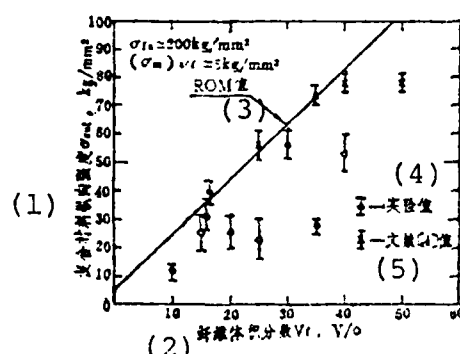

Fig. 7   Relationship of the composite's longitudinal strength and volume fraction.

   Key: (1) Composite's longitudinal strength; (2) Fiber's volume fraction ; (3) Value; (4) Test value; (5) Reference [4]'s value.

42

Figure 7 shows the ROM value and test value of the composite's longitudinal strength. We can see from Table 2 and Fig. 7 that the dispersion of the composite's longitudinal strength is relatively large. When comparing the test value and ROM value, that which is $\sigma_{cul}/\sigma_{culM} < 0.9$ occupies 28.6%; that which is $\sigma_{cul}/\sigma_{culM} = 0.7-0.9$ occupies 22.8%; and that which is $\sigma_{cul}/\sigma_{culM} < 0.7$ occupies 48.6%.

The strengths of the L4, L5 and L10 samples are close to the ROM value and value given in Reference [4]. We know from the fracture morphology shown in Fig. 5 seen by scanning microscope that their quality is very good and thus possess corresponding relatively high strength. However, the strengths of the L3, L6, L8, L9 and L11 samples have relatively large deviations from the ROM value. We know from the fracture morphology shown in Fig. 4 seen by scanning microscope that their quality is relatively poor and thus possess corresponding relatively low strength. Fiber lamination, non-uniform distribution, fiber crushing, base body looseness and other defects appear in the composite. The major reasons for this are the result of the improper use of the raw materials, the arrangement technique and the pressing infiltration parameters (temperature and pressure). The three above mentioned factors are the key as to whether or not we can obtain a composite with very good quality and relatively high strength. Therefore, it must be carefully selected and strictly controlled.

6.2 Transverse Strength

The calculation formula proposed by M.J. Klein [5] for the transverse strength of a fiber one directional reinforced metal composite is:

$$\sigma_{cut} = \sigma_{mu}/SCF$$

In the formula, σ_{mu} is the tensile strength of the base body and SCF is the stress concentration factor. Its value is

$$SCF = \frac{1 - V_f\,(E_m/E_f)}{1 - \left(\frac{4V_f}{\pi}\right)^{\frac{1}{2}}(1 - E_m/E_f)}$$

In the formula, E_m and E_f separately indicate the modulus of the metal base body and fiber.
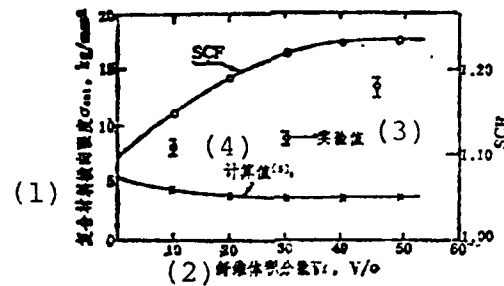

Fig. 8　Relationship between the composite's transverse strength and the fiber's volume fraction.

Key: (1) Composite's transverse strength; (2) Fiber's volume fraction; (3) Test value; (4) Calculated value.

Figure 8 shows the calculated value and test value of the composite's transverse strength. We can see from Table 3 and Fig. 8 that the test value is higher than the calculated value. This shows that the calculation formula proposed by M. J. Klein did not consider that the plastic deformation of the metal base body in the composite is necessarily constrained by the fiber [5]. When the volume fraction is below a certain value (about 0.5-0.7), the larger the volume fraction of the fiber, the larger the constraining effect of the base body. Therefore, the transverse strength of the composite is larger than the strength of the base body metal and increases with the increase of the fiber's volume fraction.

6.3　Interface Strength

It is divided into interface shearing strength (γ_i) and

interface tensile strength (σ_i). The former influences the longitudinal strength of the composite [7] while the latter influences the transverse strength of the composite. It is very difficult to measure the interface shearing strength and interface tensile strength of a composite with a fiber diameter of only ten odd micron. Here, we are only able to make a simple estimation.

We can use the following estimation for the interface shearing strength:

$$2\pi r l \tau_i = \pi r^2 \sigma_{fu},$$
$$\tau_i = \frac{r\sigma_{fu}}{2l} = \frac{d_f\sigma_{fu}}{4l}$$

In the formula, d_f is the fiber's diameter; σ_{fu} is the fiber's tensile strength; l is the fiber's pull out length on the fracture; $\sigma_{fu} \approx 200 kg/mm^2$. The l/d_f value is calculated from Fig. 5, the maximum value is 5 and when we substitute in the above formula we obtain

$$\tau_i = \frac{\sigma_{fu}}{4\frac{l}{d}} \approx 10 kg/mm^2$$

Measurement of the interface tensile strength is even more difficult. As for the composite which we developed, we still have no way of determining just how large the σ_i is. We can see from Fig. 9 that under transverse load effects, the stress on the interface is the function of θ, that is, when $\theta = 0°$, the positive stress has a maximum value and its stress concentration coefficient (σ_{max}/σ_{av}) can reach 1.5. When $\theta = 70-90°$, it changes to a negative value, that is, it becomes pressure stress. We can see that the interface destruction first must begin from the $\theta = 0°$ area (see Figs. 6a, c, d) and afterwards propagates to the two sides. From observations on the transverse

45

test piece fracture of the proportion between the interface destruction area and base body destruction area, we inferred that the interface tensile strength and base body strength are close.

Conclusion

We can make the following several conclusions from experimental research on silicon carbide fiber reinforced aluminum composite made by the pressing liquid-infiltration in vacuum method.

1. Pressing liquid-infiltration in vacuum is a relatively good method for making bundle wire continuous silicon carbide fiber reinforced aluminum. When this method was used to make the fibers, they had no noticeable damage, distribution was relatively uniform and the composite plate had very good interface joining.

2. Whether or not pressing liquid-infiltration in vacuum can make a composite with good quality and performance hinges upon the mastering and control of the pressing infiltration technique. Among these, pressure infiltrating temperature and pressure have decisive influences.

3. The pressing liquid-infiltration in vacuum technique must only be mastered and controlled well to be able to make a composite with very good quality and performance. Its longitudinal tensile strength can reach the theoretically calculated (ROM) value and its transverse strength is higher than the calculated value and also higher than the base body strength. Moreover, it enlarges with the increases of the fiber's volume fraction. This is the result of the fiber having constraining effects on the base body deformation.

4. Interface joining is mechanical joining and the interface shearing strength and tensile strength are both close to the strength of the base body metal.

References

[1] Yajima, S. et al, J. Mater.Sci., 15(1980), No.8,2130.

[2] "The Application of a New and Developing Structural Material-Metal Base Composites", Journal of Aeronautical Materials, 1981,No.1,35.

[3] Lare, P,J. et al, AD 736973, 1971.

[4] Yajima, S. et al, J.Mater.Sci.,16(1981),3033.

[5] Klein, M.J., Composite Materials, Vol.1, Chap.5, p.167, Academic Press, New York and London, 1974.

[6] Paton, W. and Lockhart, A., Factors Affecting the Transverse Stength of Fiber-Reinforced Metals, NEL Report, 1971,475.

[7] Metcalfe, A.G. and Klein, J.J., Composite Materials, Vol.1, Chap.4, P.126, New York and London, 1974.
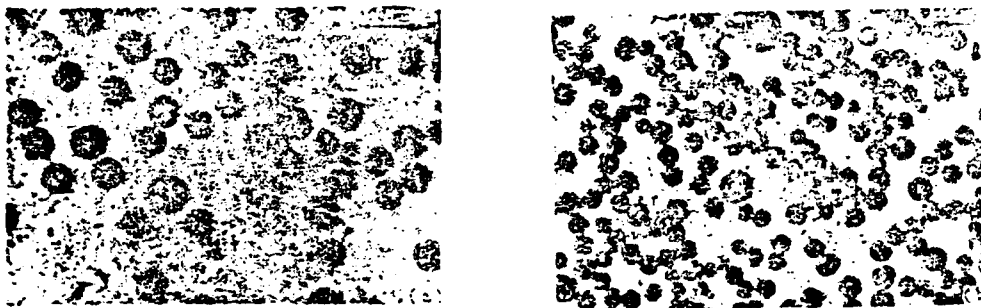
Fig. 3   Metallographic photographs of composites with different
          volume fractions.

(a) $V_f \approx 18V/0$; (b) $V_f \approx 40V/0$.
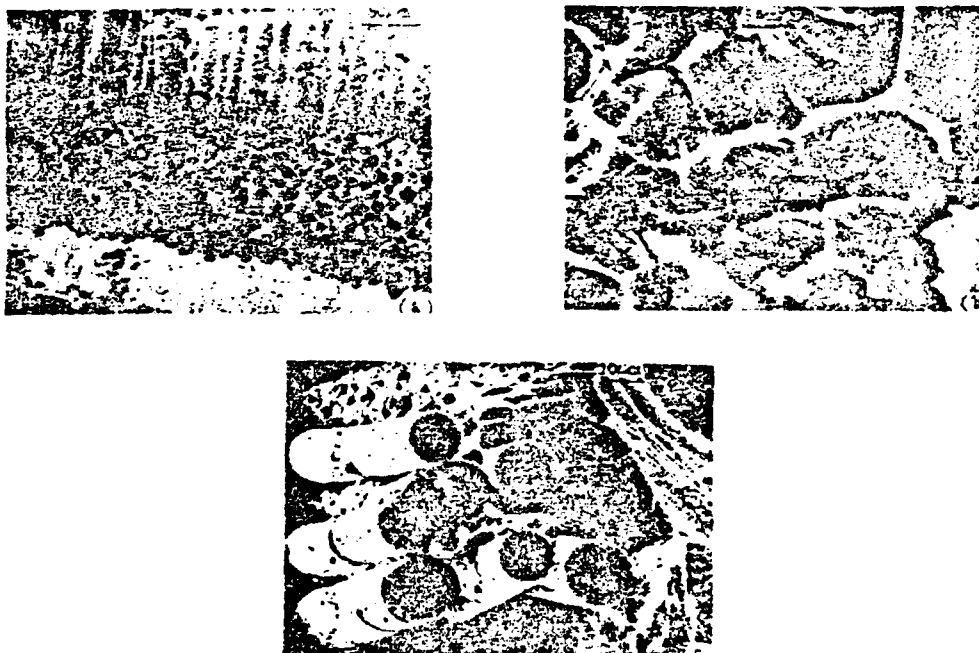
Fig. 4   Fracture morphology of composite (each type of defect).

Key: (a) Fiber lamination, scanning electron microscope;
(b) Fiber damage, scanning electron microscope; (c) Base
body looseness, scanning electron microscope.
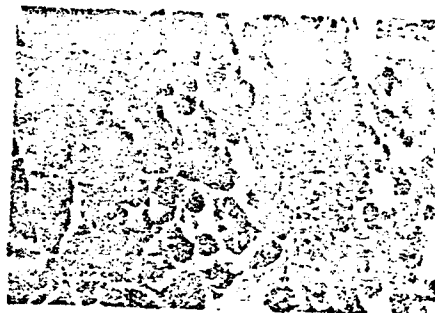
Fig. 5   Fracture morphology of composite (quality is relatively
         good).

         Key: (a) Fracture morphology using an L5 scanning micro-
         scope; (b) Fracture morphology using an L10 scanning
         electron microscope.
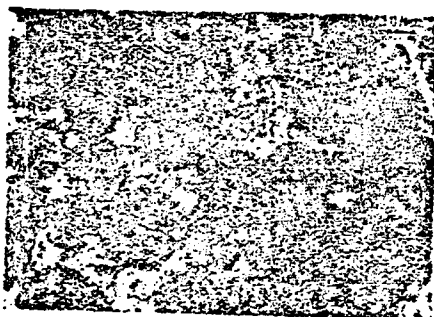
Fig. 6   Transverse fracture metallographic and scanning electron
         microscope photos.

         Key: (a) Interfacial fracturing; (b) Fracturing begins in
         fiber breaking area; (c) Transverse fracture morphology
         using a scanning electron microscope; (d) Transverse fracture
         morphology using a scanning electron microscope.

49

Fig. 9 Relationship between transverse stress and θ .

Key: (1) Stress concentration coefficient; (2) Elastic;
(3) Plastic; (4) Degrees.

50

EFFECTS OF MINOR ALLOYING ON THE SOLIDIFICATION PROCESS OF
ALLOY K5

Zheng Yuanrong, Cai Yulin and Gao Ping

Abstract

This paper studies the K5 alloy with single crystal compos-
ition and using this as the basis we separately add in the
solidification sequence of the four primary phases of MC, M_3B_2,
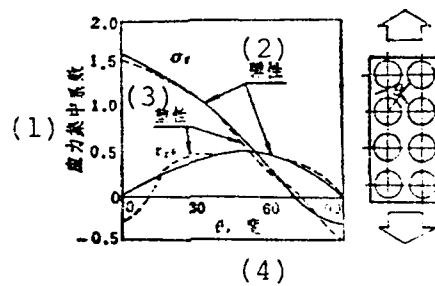eutectic $(\gamma + \gamma')$ and Ni_5Hf in alloys of carbon, boron and
hafnium, determines the solid-liquid ratio of these four types
of alloy in the solid-liquid range at different temperatures
and investigates the effects of carbon, boron and hafnium on
the solidification process.

Research results show that boron and hafnium cause the alloy
to form a M_3B_2 and Ni_5Hf low melting point phase during the
solidification process noticeably enlarges solid-liquid range of
the alloy and causes the interdendritic liquid to maintain
connection in a very wide temperature range thus raising the
castability of the alloy. The effects of carbon on the solid-
ification characteristics of the alloy is not great yet carbon
has noticeable effects on the carbide precipitation of alloys
containing hafnium. Aside from the precipitation $MC_{(1)}$ rich in
titanium above 1270°C, $MC_{(2)}$ rich in Hf also precipitates below
1240°C.

I. Preface

The structure and properties of cast nickel base high tem-
perature alloys is determined by the solidification conditions
during the solidification process. Heat treatment does not
cause large changes of the structure and properties and thus
many alloys are used in the cast state. Because of this, the

51

rational control of the alloy's solidification process and selection of appropriate casting technique parameters have important significance for obtaining high quality castings.

In recent years, much research work has been done centered on the solidification and liquid phase changes of alloys [1-5]. These are of great help in clarifying the solidification sequence of alloys, explaining the effects of microelements and appraising the castability of casted high temperature alloys. However, these works lack systematic research on the effects of boron and hafnium on the general behavior of casted alloy solidification. At present, the liquid precipitation of MC$_{(2)}$ carbide rich in hafnium has still not been determined. This paper studies the precipitation sequence of the solid-liquid ratio of K5 alloy containing carbon, boron and hafnium during the solidification process and then proceeds to investigate the effects of these elements on the solidification of casted high temperature alloys.

II. Test Material and Method

The material used is the one furnace low carbon K5 mother alloy. On this basis, we add different quantities of carbon, boron and hafnium to obtain the four furnace alloys of A,B, C and H. See Table 1 for their compositions.

(1) 合金	Zr	Co	Cr	Al	Ti	W	Mo	Ni	C	Hf	B
A	0.096	10.0	10.34	5.5	2.26	4.8	3.66	余 (2)	0.014	—	< 0.01
B									<0.01	—	0.11
C									0.17	—	0.025
H									0.15	1.30	0.002

Table 1 Chemical compositions of four furnace alloys.
Key: (1) Alloy; (2) Remainder.

The melted test sample is imbedded in a piece of graphite and is surrounded and filled with a silicon sol corundum coating. After drying, it is placed in a silicon carbon tube furnace, heated to 1370°C and the temperature is maintained for 10 minutes causing the sample to completely melt. It is then cooled to different temperatures for 15 minutes and afterwards tempered in water. The maintained temperature range was 1350-1100°C with an interval of 20°C.

The differential thermal analysis was carried out on the Daojin DT-2A instrument, platinum was selected as the reference sample and the rising temperature rate was 10°C/minute.

After isothermal solidification, the sample was analyzed by the metallographic, quantitative metallographic, scanning microscope, energy spectrum and electronic probe etc. methods to determine the solid-liquid ratio and the solidification sequence of each phase.

III. Test Results

3.1 Differential Thermal Analysis

Figure 1 is the curves of the differential thermal analysis (DTA) of four types of alloys. Figure 1a is the result of alloy A. Without the effects of carbon, boron and hafnium, there are only the two peaks of 1280-1363°C and 1355-1210°C on the differential curve which indicate alloy melting and solidification.
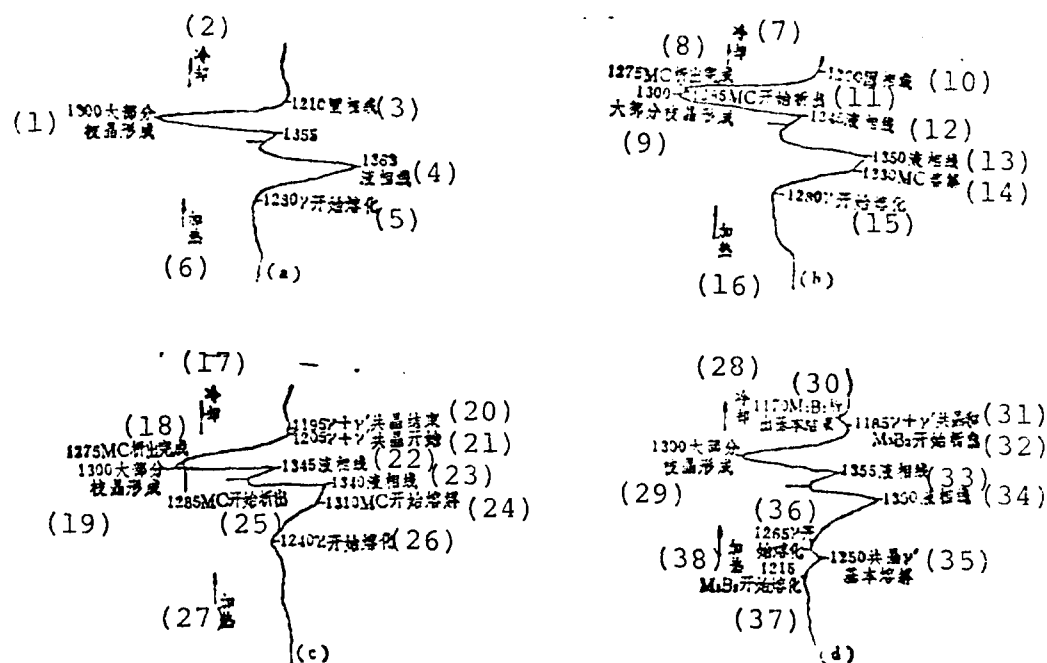
Fig. 1 Differential thermal analysis curves of four types of alloys.

Key: (1) Majority has dendrite forming; (2) Cooling; (3) Solid phase line; (4) Liquid phase line; (5) Begin melting; (6) Heating; (7) Cooling; (8) Precipitation completed; (9) Majority has dendrite forming; (10) Solid phase line; (11) Begin precipitation; (12-(13) Liquid phase line; (14) Solution; (15) Begin melting; (16) Heating; (17) Cooling; (18) Precipitation completed; (19) Majority has dendrite forming; (20) Eutectic finished; (21) Eutectic begins; (22)-(23) Liquid phase line; (24) Begin fusion; (25) Begin precipitation; (26) Begin melting; (27) Heating; (28) Cooling; (29) Majority had dendrite forming; (30) Precipitation basically finished; (31) Eutectic and...; (32) Begin precipitation; (33)-(34) Liquid phase line; (35) Eutectic γ' basically fused; (36)-(37) Begin melting; (38) Heating.

Because alloy C has 0.17% C, the MC carbide fusion and precipitation peaks superposed on the differential curve γ melting and solidification peaks cause the top peak of the γ peak to

54

distort (Fig. 1b).

Alloy B is a BC type alloy with low carbon and high boron. It has one more peak in the 1215-1250°C area on the differential curve as compared to the A and C alloys. This peak indicates the melting of M_3B_2 and eutectic γ' (Fig. 1c). The M_3B_2 phase is a type of eutectic phase with a low melting point. The corrosion and induction of its melted pool on the eutectic γ' causes eutectic γ' to melt. If there is no induction of M_3B_2, eutectic γ' will gradually dissolve into the γ base body in a very wide temperature range but is unable to obtain a sharp peak on the differential curve which reflects eutectic γ' melting. Further, because of the melting of M_3B_2 and eutectic γ', there is further decrease of the melting temperature of the γ base body and A alloy drops from 1280°C to 1265°C.

Alloy H contains 1.8% Hf and 0.15% C. During the heating process, the action of the hafnium causes the γ melting temperature to decrease from the A alloy's 1280°C to 1240°C. The melting and precipitation peaks of the Ni_5Hf phase do not appear on the differential curve. This is because it has a relatively small quantity and continually becomes a solid solution during the heating process. However, during the melting process, it has inducing effects on the melting of eutectic γ' and the base body. The adding in of hafnium noticeably increases the quantity of eutectic γ' and therefore the precipitation peak of eutectic γ' appears in the 1205-1195°C temperature range of the H alloy's cooling curve.

(1)合金	(2)加 热			(6)冷 却		
	(3)液相线	(4)固相线	(5)温度区间	(7)液相线	(8)固相线	(9)温度区间
A	1363	1280	83	1355	1210	145
B	1350	1215	135	1355	1170	185
C	1350	1280	70	1345	1200	145
H	1340	1240	100	1345	1195	150

Table 2 Main temperatures (°C) of four types of alloys.

Key: (1) Alloy; (2) Heating; (3) liquid phase line; (4) Solid phase line; (5) Temperature area; (6) Cooling; (7) Liquid phase line; (8) Solid phase line; (9) Temperature area.

Table 2 synthesizes and obtains the solid phase line and liquid phase line temperatures of four types of alloys. We can see that during heating and cooling, the peak temperatures of the differential curves do not coincide. The peak temperatures during solidification is often pushed to an even lower temperature. This is due to the even faster speed (20°C/minute) of the differential analysis cooling and therefore the liquid precipitation of the phase has an even larger degree of super-cooling. On the other hand, because the melting and solidification processes are irreversible, diffusion in a solid state occurs in the heating process which causes the phases of the metals (e.g. eutectic γ') to gradually become solid solutions. This process often causes the melting temperature of the alloy to be pushed to a high temperature. During the cooling process, the cast alloy generally uses the L $\rightarrow$ γ + γ' eutectic reaction to complete the entire solidification process. When large quantities of Ni_5Hf and M_3B_2 exist in the alloy, after the (γ + γ') eutectic reaction is completed, the Ni_5Hf and M_3B_2 also precipitate and further expand in the solidification area.

3.2 Isothermal Solidification

The carbon and boron contents in the A alloy are very low and therefore the major primary phases of this alloy are the γ solid solution and eutectic γ'. Isothermal solidification tests show that the alloy still did not begin solidification at 1360°C but already solidified 33.7% at 1350°C. Following the lowering of temperature, the dendritic development of the solidification was very fast and when it reached 1310°C the alloy had already solidified 90%. At a temperature of 1290°C, the alloy's interdendritic liquid had formed a disconnected state (Fig. 2a, see Plate 9). Before the precipitation of eutectic γ', the residual liquid pool independently scatters on the γ base body (Fig. 2b, see Plate 9) up until the 1240°C alloy uses the $L \rightarrow \gamma + \gamma'$ eutectic reaction to complete the entire solidification process.

The main primary phases of the C alloy are the γ solid solution, MC carbide and eutectic γ'. At 1360°C, the alloy is 100% liquid, at 1350°C the alloy has already solidified 45.7% (Fig. 3a, see Plate 9) and at 1310°C the alloy's solidification reached 90%. In the 1360-1310°C temperature range, the solidification characteristics of the C alloy are similar to those of the A alloy and in the near 50°C temperature range, 90% of the dendrite skeleton has already formed. When this alloy is 1290°C, the distribution of the interdendritic residual liquid is the same as that of the alloy A base body. The MC carbide in the alloy noticeably precipitates at 1310°C (Fig. 3b, see Plate ()). The large pieces of MC carbide are precipitated during the isothermal process and the fine skeleton shaped carbide is formed during the quenching process. The precipitation process of the MC carbide is continued up to 1270°C and is completed there. Solidification is completed after eutectic γ' precipitation at 1235°C.

The primary phases of the B alloy are the γ solid solution,

57

eutectic γ' and M_3B_2 phases. At 1310°C, alloy solidification is about 80%. After this, when it reaches 1250°C, the alloys maintain about 10% residual liquid and do not solidify again. This section of liquid distributed within the dendrite is interconnected (Fig. 4, see Plate 9). Eutectic γ' has noticeable precipitation at 1230°C (Fig. 5, see Plate 9). Because of the results of low carbon and high boron, after the eutectic reaction at 1210°C is finished, the eutectic γ' quantity increases from 2% of the A alloy to 5.5% of the B alloy. At 1230°C, M_3B_2 has no local precipitation of eutectic γ' (indicated by the arrow in Fig. 5), yet in the liquid pool on the boundary of eutectic γ' a large amount of boride is still not precipitated. It is precipitated by the rediffusion method (indicated by double arrows in Fig. 5). This proves that the existence of eutectic γ' causes the M_3B_2 precipitation temperature of the final crystal to decrease. In the same way, the existence of M_3B_2 also decreased the temperature of the $\gamma + \gamma'$ beginning eutectic and the 1240°C of the A alloy without boron dropped to the 1230°C of the B alloy containing boron. Finally, at 1210°C isotherm, the residual liquid used the $L \rightarrow \gamma + M_3B_2$ reaction to complete the entire solidification process (Fig. 6, see Plate 10).

Aside from the γ solid solution, the primary phase of the H alloy also has the $MC_{(1)}$, $MC_{(2)}$, eutectic γ' and NiHf phases (Fig. 7, see Plate 10). At 1350°C, this alloy also has beginning solidification yet at 1345°C it has already solidified 40% and at 1310°C the alloy solidified 61%. In the very wide temperature range of 1310-1250°C, the $MC_{(2)}$ carbide begins to precipitate in the alloy (Fig. 8a, see Plate 10) and continues to react until 1270°C where it is finished. The hafnium rich $MC_{(2)}$ begins to precipitate in the alloy at 1240°C and this type of carbide often appears on the boundary of eutectic γ'. Sometimes it appears alone and sometimes together with $MC_{(1)}$ (Fig. 8b, see Plate 10).

After eutectic γ' precipitates, at 1190°C, the boundary of eutectic γ' still has a liquid pool rich in 1% hafnium. It continues to 1150°C whereupon the alloy is completely solidified. Because isothermal solidification is used, the small amount of Ni_5Hf formed in the alloy becomes a solid solution at a maintained temperature and enters the base body or transforms into hafnium-rich $MC_{(2)}$ (Fig. 9, see Plate 11). Therefore, after isothermal solidification, the alloy does not have an Ni_5Hf phase.

In order to determine the composition of the primary phase of the H alloy, we used an electronic probe to analyze the sample after 15 minutes of isothermal solidification at 1210°C. The results are listed in Table 3.

(1) 相 分子式	(2) 位置 编号	(3) 各相中主要成分（重量%）							
		Cr	Al	Ni	Ti	Mo	W	Hf	Co
$MC_{(1)}$	1	1.3182	0.0000	2.0655	31.3672	15.0212	30.4650	3.6380	0.2713
(4) 分子式	$(Ti_{0.616}W_{0.156}Mo_{0.147}Ni_{0.033}Cr_{0.024}Hf_{0.023}Co_{0.004})C$								
$MC_{(2)}$	2	0.5250	0.0000	2.2408	4.0972	2.6602	4.4836	69.9096	0.7059
(5) 分子式	$(Hf_{0.664}Ti_{0.145}Ni_{0.065}Mo_{0.048}W_{0.041}Co_{0.020}Cr_{0.017})C$								
(6) 等温γ'	3	4.7680	6.7175	70.2493	3.7014	1.8482	1.6724	2.4110	7.1133
(7) 淬火γ'	4	3.6378	6.8211	70.3023	3.7528	1.3238	1.4581	3.4281	6.4706

Table 3   Results of the determination of the composition of the primary phase in H alloy using an electronic probe.

Key: (1) Phase molecular formula; (2) Position number; (3) Main composition of each phase (weight %); (4)-(5) Molecular formula; (6) Isothermal; (7) Quenched.

See Fig. 10 (see Plate 11) for the fixed point analysis positions of each phase by the probe. The distribution chart of the surface of each phase's composite elements is as shown in Fig. 11 (see Plate 11). Aside from this, we also used the energy

spectrum to quantitatively analyze the compositions of the two types of carbides, $MC_{(1)}$ and $MC_{(2)}$. The result was that these two types of carbides can be separately indicated by $(Ti_{0.576}W_{0.212}MO_{0.150}Hf_{0.062})C$ and $(Hf_{0.717}Ti_{0.194}W_{0.054}M_{0.035})C$. By comparing this with the results in Table 3, we can know that the two basically agree, that is, $MC_{(1)}$ is dominated by titanium and $MC_{(2)}$ is dominated by hafnium.

We can also see from the data in Table 3 that whether eutectic γ' precipitates in the isothermal solidification process or eutectic γ' precipitates in the quenching process, the compositions are very close. This shows that the effects of the changes of the solidification conditions on the composition of eutectic γ' are very minor.

We determined the solid-liquid ratio of isothermal solidification of the various alloys under different temperatures for the quantitative metallographic analysis of samples of four types of alloys with various solidification states. The results are shown in Fig. 12.
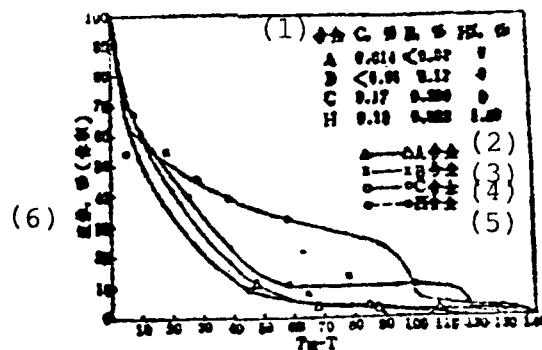

Fig. 12   Chart of the liquid % when there is solidification of
         four types of alloys -- the (T liquid - T) relationship.
         Key: (1)-(6) Alloy.

We can see from Fig. 12 that during the initial period of

solidification these four types of alloys have similar characteristics. That is, during the initial stage of solidification, the solidification speed is very fast in the 40°C range and in this stage, based on the different alloys, 60-90% of the liquid has already been solidified. However, during the later period of solidification, the differences of the solidification characteristics of the different alloys are very large. In a very wide temperature range, alloys with high boron and containing hafnium maintain relatively high amounts of liquid and even cause the later period solifification to maintain a halted state.

IV. Discussion

For a long time, when people appraised the castability of casted high temperature alloys, they considered reducing the elements of the solidification range was beneficial to raising the castability of alloys. However, at the end of the 1960's, the method of high boron and added hafnium which was used to raise the medium temperature strength and plasticity of high temperature alloys greatly enlarged the solid-liquid range. Afterwards, further research on this type of alloy showed that even though the solidification range of this type of alloy is very wide, yet their tendency to form looseness and thermal cracks greatly decreased especially for alloys containing hafnium where the thin wall performance was especially good. This phenomenon appears to be in contradiction to the traditional view.

In high temperature alloys, during alloy solidification, the higher the temperature of the ability to lose interdendrite complementary reduction the wider the solidification range, and the greater that section which lost the complementary reduction ability, the worse the castability of the alloy. At 1290°C, the A and C alloys lose their abilities for interdendritic complementary reduction. At this time, the residual liquid quantities

these two types of alloys are separately 3.8 and 7.9%. When this part of the liquid continuously solidifies, because the solidification shrinkage possibly forms looseness, it is finished at 1240°C when the residual liquid uses the $L \to \Upsilon + \Upsilon'$ eutectic reaction. In the 1290-1240°C temperature range, because of the existence of liquid in the alloy, its strength and plasticity are very low. If the shape of the part's section is complex, the heat stress caused by solidification exceeds the strength of the alloy in this state and thus easily produces heat tears. Most of the samples quenched in this temperature range show cracks but this is circumstantial evidence.

The solidification characteristics of alloys with boron and hafnium is another matter. Before they reach 1230°C eutectic Υ' precipitation, they maintain a relatively good interdendritic connected state. The complementary reduction effects within the dendrite greatly decrease the loosening tendency of the alloy. Aside from this, these liquids which maintain relatively low temperature are beneficial to loosening the thermal stress of the alloys produced during the cooling process and decreasing the heat cracking tendency.

We should pay attention that when the quantity of the residual liquid is 8%, the interdendritic liquid pools of the A and C alloys are disconnected from eachother yet those of the B and H alloys are connected. This is naturally related to the characteristics of the final solidified liquid itself. Eutectic liquids containing hafnium and boron have very low melting points, very good flow and soaking abilities, can form very thin liquid film within the dendrite and give full effect to the interdendritic capillaries. This type of eutectic liquid which does not reach eutectic temperature is unable to gradually crystallize.

We can know from the above analysis that to reduce the tendencies of looseness and heat cracking, it is necessary to change the

characteristics of the final solidified liquid pool. One method is to eliminate the alloy's eutectic γ' which causes the alloy to completely solidify at 1290°C. We can also attain this goal by decreasing the alloy's aluminum and titanium contents or eliminating the boron and zirconium. Another method is to increase the amount of eutectic γ' which causes the interdendritic liquid before eutectic γ' precipitation to maintain a connected state. We can also attain the goal by adding hafnium or low carbon and high boron.

When we compare the two above mentioned methods, the potential of the latter is even greater. This is because, as regards high strength casted high temperature alloys, eutectic γ' is a commonly existing phase and eliminating it signifies a decrease of the alloying level and it effects the mechanical properties of the alloy. Further, the effects of the technical factors on the precipitation of the eutectic γ' in the alloy are very sensitive. Alloys which originally had no eutectic γ' can also appear when there is fast speed solidification. Therefore, this type of alloy has poor adaptability to the technique during cast production. The latter method is not the same. Under the premise of maintaining the alloy's high alloying, whether or not the composition or technique changes in a very wide range, it can always obtain a connected state and obtain excellent castability. Therefore, this type of alloy has strong adaptability to the technique and is especially suitable for thin wall forgings.

5. Conclusion

1. The effects of boron and hafnium on the solidification characteristics of K5 alloy are very similar. They decrease the liquid phase line and solid phase line of the alloy and enlarge the solidification temperature range. The decrease of the solid phase line is even more noticeable.

63

2. In alloys which do not contain boron and hafnium, the alloys use the $L \rightarrow \gamma + \gamma'$ eutectic reaction to complete the solidification process but alloys with boron and hafnium separately use $L \rightarrow \gamma + M_3B_2$ and $L \rightarrow \gamma + Ni_5Hf$ to complete the solidification process of the alloy.

3. The eutectic γ' precipitation temperature of alloys with boron and hafnium decreases and before the $L \rightarrow \gamma + \gamma'$ eutectic reaction a relatively large amount of liquid is maintained in a very wide temperature range. This causes this type of alloy to have excellent castability.

4. The addition of carbon only slightly decreases the liquid phase line of the alloy and it has no noticeable effects on the solid phase line.

5. The hafnium-rich $MC_{(2)}$ carbide formed by the joint effects of carbon and hafnium is a low melting point phase and its precipitation temperature is 1240°C.

References

[1] Fu Hengzhi: Solidification Characteristics of the Non-Equilibrium State of High Temperature Alloys, Journal of Northwestern Polytechnical University, 1978, No.1,119.

[2] Institute of Metals: Solidification Process and Segregation of a Type of Nickel Base Casted Alloy, Papers of the First Meeting of the All-China High Temperature Alloy Conference, 1979,9.

[3] Institute of Metals: Loosening in Boron and Nickel Base High Temperature Alloys, Papers of the Second Meeting of the All-China High Temperature Alloy Conference, 1981,11.

[4] Ouichou, L.,et al, Superalloys 1980, Proc.4th Int.Symp. on Superalloys,Ed.by J.K.Tien, et al,ASM Metal Park,Ohio,1980.P235.

[5] Burton,C.J.,Superalloys,Metallurgy and Manufacture,Proc.3rd Int. Symp. on Superalloys,Ed.by B.H.Kear,et al,Claitor's Pub., Baton Rouge, Louisiana, 1976,P147.
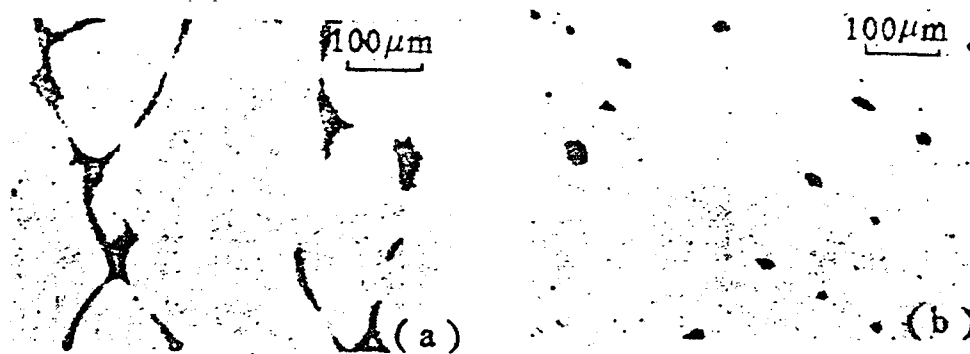
Fig. 2   Structure of alloy A after 1370°C/10 minutes + 1290°C/
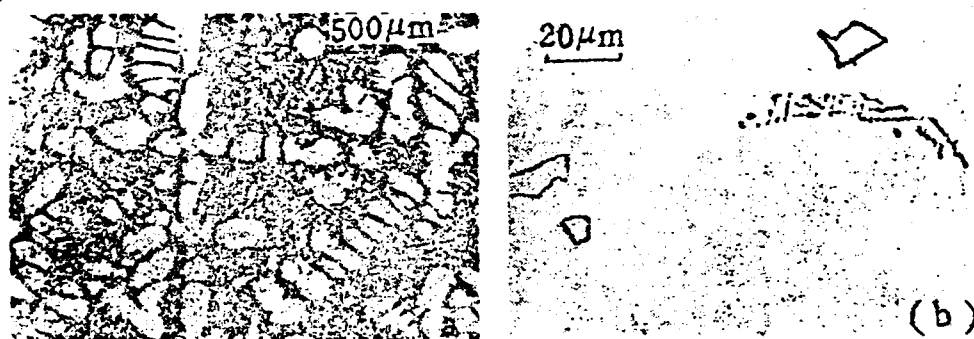15 minutes (a) and 1370°C/10 minutes + 1250°C/15 minutes
(b).

Fig. 3   Structure of alloy C after 1370°C/10 minutes + 1350°C/
15 minutes and 1370°C/10 minutes + 1310°C/15 minutes
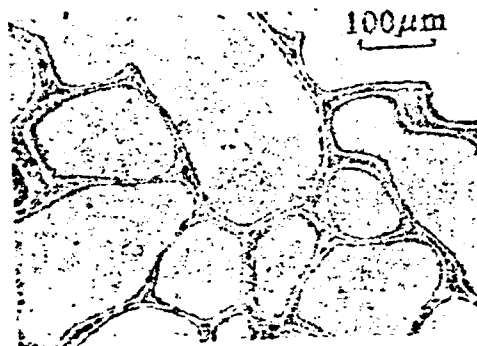quenching (b).

Fig. 4 Distribution of interdendritic liquid of alloy B after
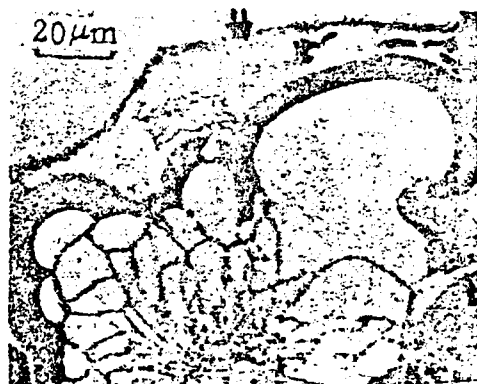1370°C/10 minutes + 1270°C/15 minutes.

Fig. 5 Structure of alloy B after 1370°C/10 minutes + 1230°C/
15 minutes quenching.

Fig. 6   Structure of alloy B after 1370°C/10 minutes + 1210°C/
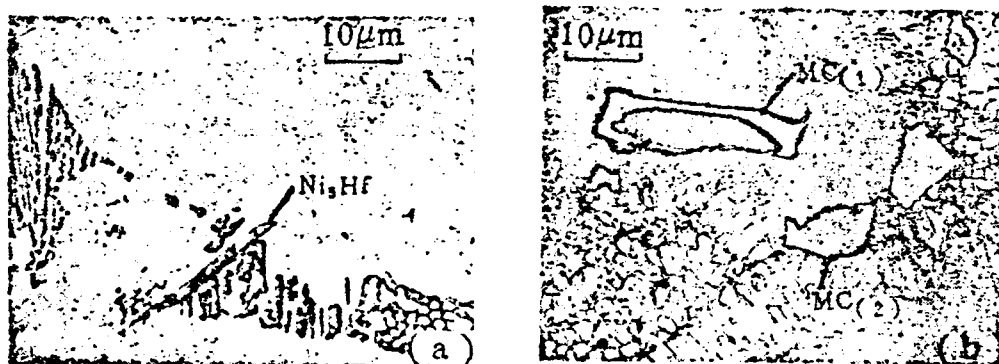15 minutes quenching.

Fig. 7 Ni_5Hf (a) and $MC_{(1)}$ and $MC_{(2)}$ carbides (b) in H alloy
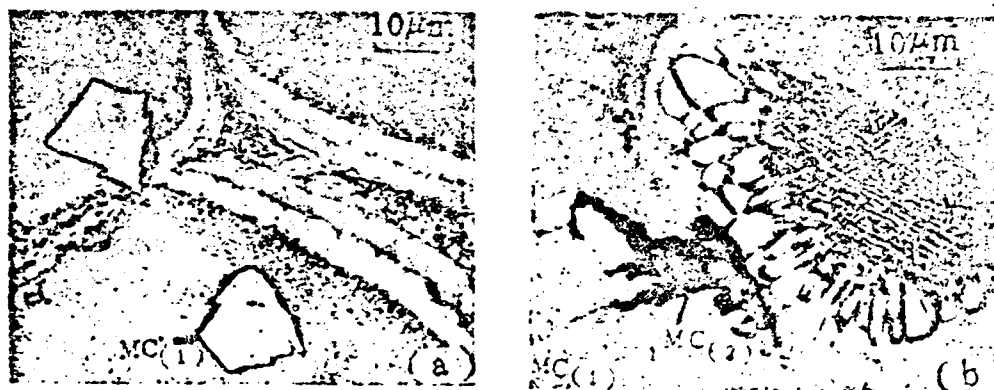casted state structure.

Fig. 8   Isothermal precipitation of $MC_{(1)}$ and $MC_{(2)}$ carbides in H alloy.

Key: (a) When temperature is maintained above 1250°C there is only $MC_{(1)}$; (b) When temperature is maintained at 1230°C there is $MC_{(1)}$ + $MC_{(2)}$.

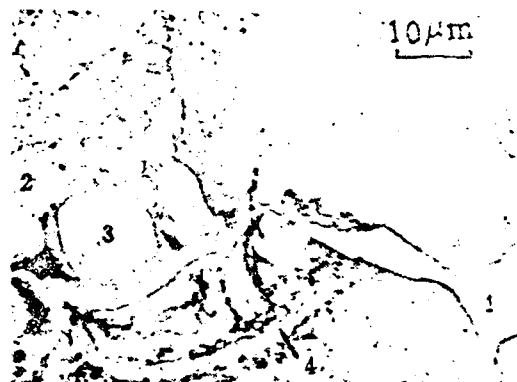Fig. 9   Eutectic γ' and $MC_{(2)}$ after H alloy quenched at 1370°C/ 10 minutes + 1150°C/15 minutes.

Fig. 10 Electronic probe's precipitation position after quenching
of H alloy at 1210°C.

Key: (1) $MC_{(1)}$; (2) $MC_{(2)}$; (3) Isothermal precipitation γ';
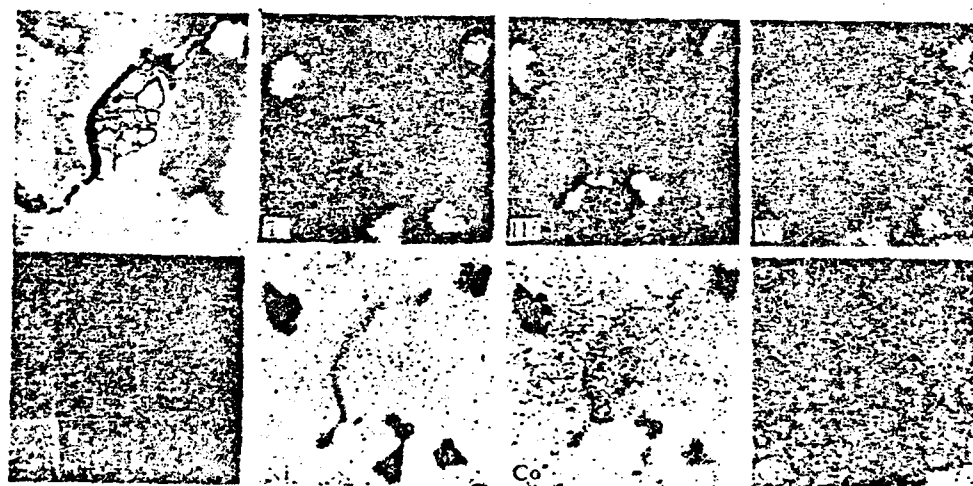(4) Quenched and precipitated eutectic γ'.

Fig. 11 Distribution of the surface of each element in $MC_{(1)}$
and $MC_{(2)}$ after H alloy quenching at 1210°C.

69

THE INFLUENCE OF EPOXY RESINS WITH DIFFERENT MOLECULAR WEIGHTS
ON THE CURING PROCESS AND THE PROPERTIES CF COMPOSITES

Nie Jianyang, Xie Shufang and Yu Zhennan
Beijing Research Institute of Materials and Technology

Abstract

This paper used the high power liquid color spectrum, DSC,
TGA, DMA, viscoelasticimeter and other commonly used methods to
reveal the influences of epoxy resins with different molecular
weights on the curing process and the properties of composites.
Test showed that: for epoxy resins with relatively small mole-
cular weights, the gel time was long, the flowability was
large, the initial reaction temperature and peak summit temper-
ature were high, the reaction heat was small (e.g. Martin's
heat resistance, glass transition temperature, decomposition
temperature and heat loss of weight) and the module retention
etc. at 150°C were worse than epoxy resins with high molecular
weights.

Preface

In reality, the original materials of epoxy resins in
advanced composites are a "composite system." The chemical
compositions batch processed at different times have changes.
These changes influence the chemical, physical, mechanical and
heat properties of the resin and thus necessarily influence
the forming process parameters and the stability of the com-
posite's properties and quality. Following the advances in
modern scientific technology and the practice of composite
applications, it was proved that the specification indices of
present commercially used resins are far from being able to
satisfy these requirements and that it is necessary to carry
out "fingerprint analysis" and stringently control the chemical
compositions of resins. This paper only studies one important

70

factor - the changes of various properties caused by different molecular weights and molecular weight distributions.

Test Results and Discussion

The Properties of Raw Resin

Epoxy resins are the same as other high polymers. The n value of the number of representative repetition chains are different and their molecular weights are different; the number of different n value molecules in the resin influence molecular weight distribution. See Table 1 for the production specification indices of the epoxy resin studied in this paper.

(1) 软化点 ·C	(2) 环氧值 (5) 当量/100克	(3) 有机氯	(4) 无机氯	(6) 挥发份 %	(7) 生产厂
≤70	0.46~0.53	0.08	0.005	≤2	上海 树脂厂 (8)
≤70	0.44	0.08	0.005	≤2	无锡 树脂厂 (9)

Table 1 Production specification indices of epoxy resin.
Key: (1) Softening point; (2) Epoxy value; (3) Organic chlorine; (4) Inorganic chlorine; (5) Equivalent weight/100 grams; (6) Volatile component %; (7) Production factory; (8) Shanghai Resin Factory; (9) Wuxi Resin Factory.

In reality, the chemical compositons of each batch of resin as shown in Fig. 1 have great differences and thus each of the softening points, mean molecular weights and epoxy value are different (see Table 2).

71

(1)	(2)	(3)
软化点, °C	数均分子量, $\overline{M}_n$	环氧值, 当量/100克
28	436	0.53
43	542	0.48
49	617	0.46
53	639	0.44

Table 2 Composite measurement results of different batches of epoxy resin.

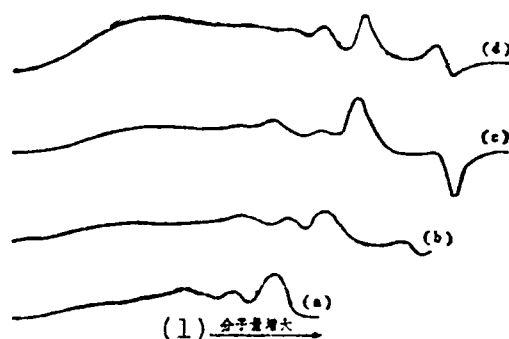Key: (1) Softening point; (2) Mean molecular weight; (3) Epoxy value, equivalent weight/100 grams.

(1) 分子量增大 →

Fig. 1 GPC distribution of different batches of epoxy resin.

Chart no.	(a)	(b)	(c)	(d)
Softening point, °C	28	43	49	53

Key: (1) The molecular weight enlarges.

The results of studying the influences of different molecular weights and molecular weight distributions under the same curing agent on the various properties of resin are as follows:

1. Gel Time

In the rising temperature process or under constant reaction temperature, the gel time of the resin branches from the line type molecular reaction and gradually thickens from the flowing state and changes into the speed of the gel state. This is one of the important reference foundations for selecting the proper pressurization moment in the composite curing process. It can be seen from Fig. 2 that for resins with different molecular

weights, the differences in gel times are very large and in the test batch resin range the gel time differences are 2-3 fold. Under the test temperatures, resins with relatively high molecular weights have fast gel speeds and those with relatively low molecular weights have relatively slow gel speeds. This creates difficulty for determing the proper moment for pressurization and it is not advantageous for the stability of the curing process.
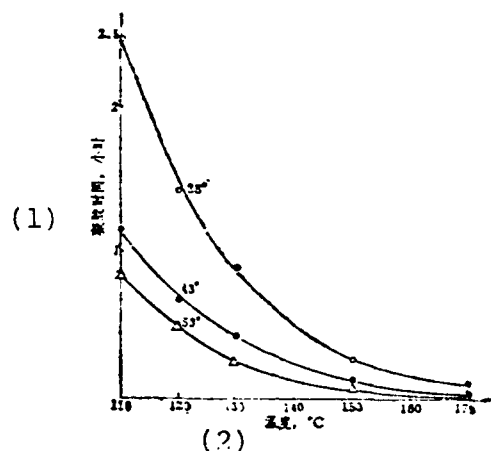
(1)

Fig. 2 Relationship of the gel time and temperature of number 648 epoxy resin.

Key: (1) Gel time, hours; (2) Temperature.

2. Flowability

The quality of prepeg materials has decisive influences on the quality of the composite. One of its indices is the flowability which points to the quantity of flow loss of resin under pressed conditions. Naturally, excessively large flowability can cause an excessive amount of flowing gel which can result in the product being deficient in gel; but when the flowability is excessively small, the pressing properties can be poor and the porosity rises; different quantities of flowing gel can cause the product's fiber volume content to become large and the various above mentioned factors can influence the properties and quality of the product. Although there are many factors

73

influencing flowability such as the resin content, volatile
component, precuring process etc., we will only discuss the
influences of resins with different molecular weights (see
Table 3). The flowability of resins with low molecular weights
is large and in the test batch resin range, the differences in
flowability are about 20%. This is difficult to use in a
stable curing process.

(1) 树脂软化点, °C	(2) 流动性, %
28	36
43	22
53	16

Table 3 Flowability of different batches of resin.
         Key: (1) Resin's softening point; (2) Flowability.

3. Characteristics of Curing Reactions

The curing reaction characteristics of epoxy resin can be
shown by the peak initial temperature (T_a), peak summit temper-
ature (T_b), peak final temperature (T_c), reaction time (τ)
and reaction heat etc. measured from the DSC curve. We can see
from the regularity results shown in Table 4 that: following
the increase of the resin's molecular weight, T_a, T_b and T_c
gradually decrease, τ lengthens and Δ H enlarges. In this,
taking T_a and T_b as most noticeable, the difference is more than
ten degrees and this will markedly influence the curing process
and product's quality.

74

(1) 树脂软化点，°C	T_1,°C	T_3,°C	T_2,°C	τ, min	ΔH, mcal/mg
28	126	187	241	116	69
43	121	176	240	115	79
49	118	175	239	120	83
53	113	171	237	125	90

Table 4   Thermal effect parameters of different batches of
resin.

Key: (1) Resin's softening point.

4.   Heat Resistance

We use a resin casting to measure the Martin's heat resist-
ance which is the heat resistance changes of resins with
different reactions (Table 5).

(1) 树脂软化点，°C	(2) 马丁耐热温度，°C
28	115
43	140
49	150
53	170

Table 5   Martin's heat resistance tempera ture of different
batches of resin.

Key: (1) Resin's softenpoint; (2) Martin's heat
resistance temperature.

We can also see the size of the deformation after sustaining
heat (Fig. 3). It is not difficult to see that: when the
resin's molecular weight increases the Martin's heat resistance
temperature noticeably rises and in the test resin range the
difference can reach 55°C; moreover, under the temperatures.
the deformation of resins with high molecular weights is
relatively small and reaching similar deformation quantity

75

temperatures the deformation of resins with high molecular weights noticeably rises. From this, we can make the following conclusions: (1) by not changing the resin system but only controlling the different molecular weights of the resins, we can satisfy the requirements for different processes and different service temperatures; (2) by not controlling the molecular weight range of the resin, we can cause the heat resistance and other property dispersion of the composite product to be too large.

5. Heat Loss of Weight

The heat resistance of a resin system can also use heat loss of weight properties to give a reaction. Figure 4 shows that the decomposition temperature of the studied resin system is 300-400°C and the decomposition temperature of resins with low molecular weights is low; when greater than 300°C, the heat loss of weight under the same temperature will be much greater for resins with low molecular weights.

6. Linear Expansion Coefficient

We can see from Fig. 5 that the linear expansion coefficient of resin is between 57×10^{-6} - $75 \times 10^{-6}/°C$ and the difference with the linear expansion coefficient of carbon fiber is very large. Moreover, each of the linear expansion coefficients of resins with different molecular weights is different and those with high molecular weights have relatively small linear expansion coefficients. From the matching properties of decreasing the stress in the composite and improving the composite with the simultaneously use of structures of other materials, we should not overlook the influences of the different molecular weights of resins.
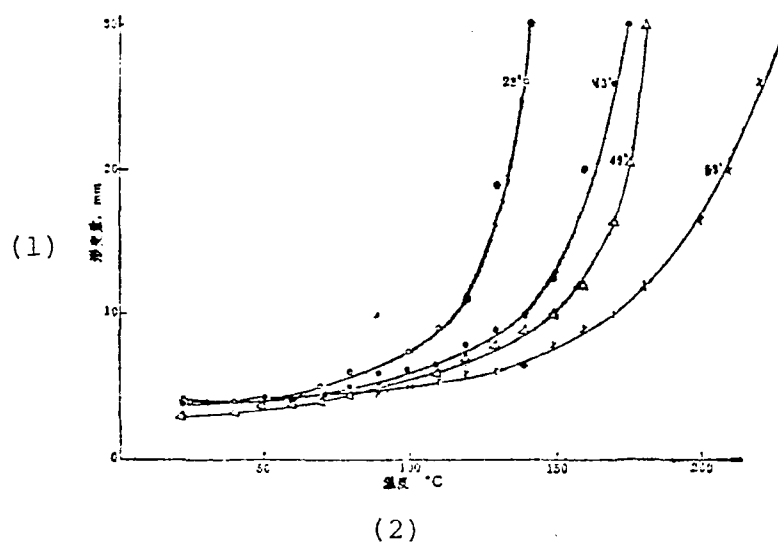
(1)

(2)

Fig. 3 Relationship of the heat deformation and temperature
of number 648 epoxy resin with different molecular
weights.
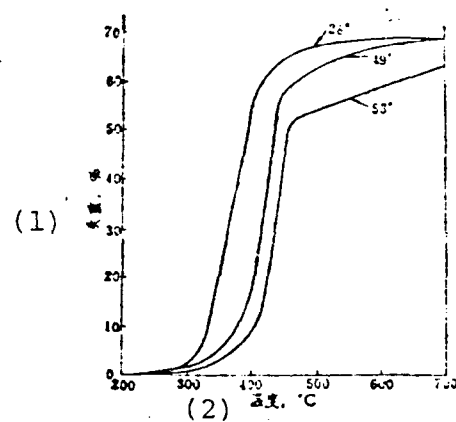
Key: (1) Deformation; (2) Temperature.

(1)

(2)

Fig. 4 Curves of heat loss of weight properties of number 648
epoxy cast resin with different molecular weights.

Key: (1) Loss of weight; (2) Temperature.
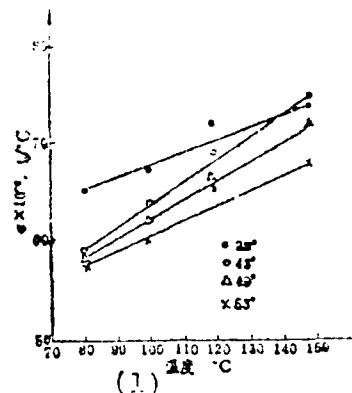
77

Fig. 5   Linear expansion coefficient of number 648 epoxy
         cast resin with different molecular weights.

         Key: (1) Temperature.

7.   Dynamic State Mechanical Properties

We can see from the Young's module temperature spectrum
(Fig. 6) of the cast resin's dynamic state measured under fixed
frequency (62.5Hz), the consumption temperature spectrum of the
mechanical properties (Fig. 7) and tables 6 and 7 that: (1) the
T_g of resins with relatively high molecular weights is high,
their laws coincide with the Martin's heat resistance tempera-
ture and the numerical values are very close; (2) whether at
room temperature or high temperature, the Young's module of
resins with high molecular weight is high and at high tempera-
tures the decrease is relatively small.   These change values
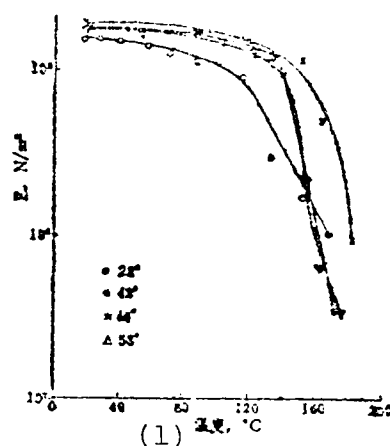directly influence the properties and quality of the composite.

78

(1)

Fig. 6   Temperature spectrum of dynamic state Young's module
of number 648 epoxy cast resin with different molecular
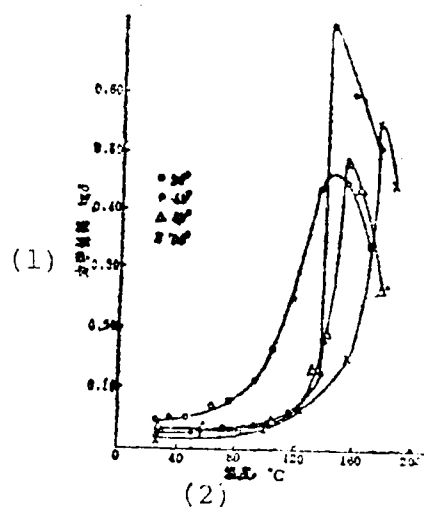weights.

Key: (1) Temperature.

(1)

(2)

Fig. 7   The mechanical consumption temperature spectrum of
number 648 epoxy cast resin with different molecular
weights.

Key: (1) Mechanical properties; (2) Temperature.

(1) 树脂软化点, ℃	(2) 玻璃化转变 T_g, ℃
28	125
43	142
49	154
53	176

Table 6 Glass transition temperatures of different batches of resin.

Key: (1) Resin's softening point; (2) Glass transition temperature.

(1) 树脂软化点, ℃	(2) 室温	100	150
28	2.1×10^9	1.3×10^9	3.1×10^8
43	2.3×10^9	2.0×10^9	3.9×10^8
49	2.4×10^9	1.93×10^9	7×10^8
53	2.75×10^9	2.1×10^9	1.1×10^9

Table 7 The Young's module ($E, N/m^2$) of different batches of resin under different test temperatures.

Key: (1) Resin's softening point; (2) Room temperature.

Conclusion

1. The influences of epoxy resin's molecular weight and molecular weight distribution on chemical, physical and heat properties are noticeable and must be controlled. Moreover, based on the utilization requirements of the composite product and the special features of the forming method, we can select resin with a suitable molecular weight range.

2. The changes which occur in the composite forming process are mainly the chemical changes of the resin system. The main

technical parameters of the forming process can be formulated
based on the change characteristics of the resin system's curing
process. There are many methods which can reflect these change
characteristics and this paper only listed the gel time, flow-
ability, the reaction's initial temperature, peak summit tem-
perature, peak final temperature, reaction time and reaction
heat etc. of the resin system. All of these are foundations for
formulating the technical parameters of curing formation. The
resin's molecular weight and the different molecular weights
which have marked influences on them directly influence the
stability of the composite forming process and the product's
properties and quality.

3. It is well known that the heat resistance and many
physical and mechanical properties of the composite are
influenced by the base body resin system. However, under the
same resin system, the serious influences caused by the chemical
composition changes of the base body resin itself is still not
fully recognized by people. This paper only points out from
research on the molecular weight and molecular weight distri-
bution that heat resistance can differ over 50 degrees and the
heat deformation quantities decomposition temperatures, heat loss
of weight, Young's module and linear expansion coefficients have
marked differences and these properties are very important for
structural composites. It can be seen that stringent control of
the resin's molecular weight and molecular weight distribution
range has important significance for guaranteeing product
quality and reliability.

4. The commonly used specification indices of epoxy resins
are unable to satisfy the quality requirements of structural
composites and it is necessary to control their chemical composi-
tions. Aside from molecular weight and molecular weight distri-
bution, among the factors influencing the resin system's
chemical composition there are also the types and contents of
the small amount of impurities in the resin, the purity of

81

solidifying agents, the impurity contents, the concentration
changes of the solidifying agents and the resin's prereaction
level etc. Because of this, when researching composites with
reliable quality and stable properties, we should carry out
"fingerprint analysis" and stringently control the quality of
the raw material and prepeg material.

References

[1] May, C.A., 24th National SAMPE symposium and Exhibition,
    24(1979), P309.

[2] May, C.A. et al, 8th National SAMPE Technical Conference
    8(o976), P274.

[3] Merrall, G.T. et al, "The Influence of Epoxy Resin Matrix
    Properties on the Performance of Carbon-fibre Composites",
    Carbon Fibres their Composites and Applications, Paper No.22,
    (1972).

[4] Shanta, P.L., "Flow of Prepregs" 18th Annual Technical
    Conference. The Society of Plastics Industry, section 8-D,
    (1963).

FATIGUE CRACK PROPAGATION IN GLASS FIBER/EPOXY RESIN COMPOSITES

Zhang Heshan, Nadeau, J.S.* and Teghtsoonian, E.*
University of British Columbia, Vancouver, B.C.

Abstract

Compact tension samples of 0/90 cross-ply non-woven and woven glass fiber/epoxy resin composites were subjected to tension-tension fatigue tests. The rate of crack propagation was monitored with a travelling microscope. We also used optical and electron microscopes to study the crack and sample sectional appearances. After burning off the resin, we also observed the crack shapes in the interior plys.

Test results show that these composites very much like some metals and plastics have the crack growth rate controlled by the applied stress intensity. The slope of the Paris curve (logda/dN versue log Δ K) for non-woven and woven composites are separately 6.8 and 10.

The fatigue crack surface appearance was found to be very different from the fast fracture surface. The former had noticeable fiber debonding and pull-out.

Preface

Composites have been widely used for making various types of structural components and these structural components are often subjected to cyclic loading. Therefore, designers must not only consider the static strength of the material but also must consider its fatigue cracking properties because the components can

83

have fractures or cracks during manufacture and use.

Many references have used linear elastic fracture mechanics (LEFM) analysis to study the fatigue crack propagation of homogeneous isotropic materials and they discovered that the fatigue crack propagation rate of material depends on fatigue stress intensity factor range $\triangle K$. Some people have proven that although the fracture process of composites are not different from that of homogeneous materials yet LEFM can be used in the same way for the fractures of composites [1-3]. The main aim of this paper is to determine the reliability of the fatigue crack propagation rate of glass fiber/epoxy resin composites on the stress intensity factor range. We also observed and studied samples with fatigue damage and searched for their special characteristics.

Tests

1. Materials and Samples
We used the following materials: (1) $[0/90]_{5s}$ cross-ply Scotchply Type 1002 single direction glass fiber/epoxy prepeg material (3M Company); (2) E fiber glass strengthened epoxy.

Based on the commercially recommended process supplied for materials, material (1) was made into plywood and the thickness of the material was about 4.20 millimeters. Material (2) was plywood supplied by the Boeing Company of Winnipeg, Canada. The thickness was about 4.15 millimeters and the direction of each ply was the same. The critical stress intensity factor K_{1c} of the two above mentioned materials were separately 32.2 and $16.2 \text{MNm}^{-3/2}$

The plywood was processed into compact tension samples as shown in Fig. 1. The outer ply fiber direction of material (1) and the radial of material (2) opposite the loading direction is 0°.

84

Fig. 1   Compact tension sample.
          Key: (1) Unit.

2.   Test Method

Before fatigue, the fracture ends of the samples used mono-
tone loading to introduce a precrack. The samples used loading
control to carry out sine tension-tension fatigue. The maximum
load P_{max} was selected on different levels based on the K_{1c} of
the material and load ratio R was between 0.05 and 0.1.
Because of the cycles under relatively high frequency, heat can
be produced in the samples [4] especially at the pointed end of
the crack. The fatigue frequency used in this study was 10Hz.

The contents of the research work include the following
three areas:

(1) The fatigue to fracture of most of the samples. We
used a microscope to observe the surface cracks so as to moni-
tor the propagation of the fatigue cracks. The typical results
are as shown in Fig. 2. For material (1), we could more clearly
see the crack positions and during observations we should cause
the light rays to pass through the sample so as to display the
dimensions of the dark area and darkest area, that is, the
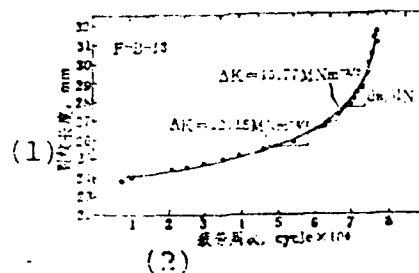length of the crack.

85

Fig. 2 Typical results of crack propagation during the fatigue process.

Key: (1) Crack length; (2) Fatigue cycle number.

(2)   We caused fatigue of the sample to have a certain length crack and then burned off the resin in the sample. Afterwards, we carefully tore off each ply in succession and observed the damage of each interior ply.

(3) We used an optical microscope to observe the fracture surface morphology of samples after fatigue fracturing.

3.   Data Processing

E.M. Wu pointed out [1] that fracture mechanics can be used for isotropic materials. Based on LEFM, the crack propagation is controlled by stress intensity factor K. The relationship between the K value, crack length a and applied stress σ is:

$$K = Y\sigma\sqrt{a} \qquad\qquad (1)$$

In the formula, Y is a parameter which is determined by the crack's geometrical shape and loading method.

The method of fracture mechanics can also be used for fatigue crack propagation. Each cycle of crack propagation da/dN is controlled by stress intensity factor range ΔK. For metallic materials, the typical relationship between da/dN and ΔK is [5]:

86

$$da/dN = A(\triangle K)^m \qquad (2)$$

In the formula, A and m are constants.

The K value of the sample used in this paper was calculated by the following formula [6]:

$$K = \frac{P\sqrt{a}}{WT} \; [\, 29.6 - 185.5\,(a/w) + 655.7\,(a/w)^2 - 1017.0\,(a/w)^3 + 638.9$$
$$(a/w)^4\,] \qquad (3)$$

In the formula, P is the load; a, w and T are the sample's shape parameters (see Fig. 1).

The fatigue test results of each sample are indicated by the curve in Fig. 2. The slope of the different points on the curve is da/dN. The difference of the fatigue's maximum load and minimum load was substituted into the P in equation (3) and we used this equation to calculate $\triangle$ K under each different crack length. The results are indicated by the logarithm of da/dN versus $\triangle$ K as shown in Fig. 3.
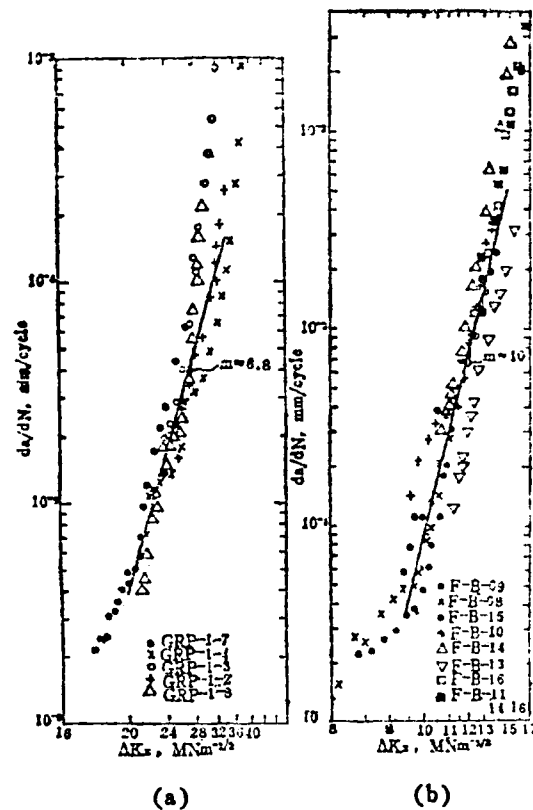
Fig. 3   Relationship of da/dN and $\triangle$K.

    (a)   1002E - glass/epoxy;
    (b)   fiber/epoxy.

Results and Discussion

    Figure 3 is the relationship of da/dN and $\triangle$K of two types
of materials.   If the metals are the same, propagation rate
da/dN of the fatigue crack is the function of fatigue stress
intensity factor range $\triangle$K.   In order to obtain the m value in
equation (2), the data used the minimum second power fitting
and obtained the m values of materials (1) and (2) to separately
be 6.8 and about 10.   Both of these were higher than the
values of most metals.

    Figure 3a shows that da/dN changes with $\triangle$K and seems to
assume three stages.   When $\triangle$K is smaller than $20 MNm^{-3/2}$,
the da/dN increasing speed is minimum; but when $\triangle$K (or K_{max},

88

because R is very small) approaches the K_{1c} value of the material (about $32MNm^{-3/2}$), the data changes very sharply. In Fig. 3b, the slope change between the second and third stages is not very noticeable yet when ΔK is lower than $9.5MNm^{-3/2}$, the da/dN increase is also relatively slow.

We can see from the obtained data that the m value of material (1) is far smaller than the m value of material (2), that is, the crack propagation of non-woven composites is far slower than woven composites. This is due to the fiber values of the former being parallel and the fiber fluctuation turns of the latter.

If A and m in formula (2) as well as primary crack length a_o and critical crack dimension a_c are known, then the fatigue life of the part can be estimated by combining formulas (2) and (1). That is, after integration, we can obtain the time required when the part breaks. We can see that the determination of the A and M values is of real significance.

As regards the 1002 composite sample, during the fatigue process, aside from the main crack's extending along the fracture direction, we can also continuously see debonded tearing, lamination and the outer surface ply is parallel to the belt shaped stripping of the load direction. Figure 4 (see Plate 12) is a photograph of the damaged form of a 1002 composite sample. Figure 4a is the surface destruction of the near final fracture of the sample. Figure 4b is two halves of a sample after fracturing. However, similar damage is not seen in woven composites.

Figures 5 and 6 (see Plate 12) show photographs of the interior plys after the resin has been burned out. Figure 5 is the typical fracture tracing of the 0° ply fiber in the $[0/90]_{5s}$ sample. The relatively weak point of the fiber is

89

randomly distributed along its length, the fracture trace does not form a straight line along the required direction but is an irregular "saw-tooth shaped" line. If the fracture traces of each ply are comprehensively considered, the effective cracks propagate along the required direction. The saw-tooth shaped traces of the different ply coincide and assume a relative dark area under penetrating light and not one clear straight line.

Figure 6 shows the fatigue crack trace of the interior ply in the woven sample. The cracks also go forward along an irregular path yet the level of fluctuation is not as large as the non-woven samples. The surface ply cracks are also the same as those of the interior ply. The fiber bundle fractures naturally produce woven intersecting points. This is because the stress concentration of these points is relatively serious.

Figures 7 and 8 (see Plate 13) show the study results of fracture surface morphology. Among the symbols in the figures, the "0" area is the fatigue fracture area, the "1" area is the fast fracture area after the crack reaches critical length and "N" indicates the top part of the machine process fracture. We can see from the figures that the fatigue fracture surface morphology is very different from the fast fracture surface. As regards fiber material (Fig. 7), the fatigue fracture surface area is quite rough, some fibers are pulled out and placed aside for a short time; but as regards the fast fracture surface, although there are also some very short fibers pulled out, yet the entire surface is still quite flat. As regards non-woven material (Fig. 8), the fibers pulled out from the fatigue crack surface area are very long and form an irregular toothbrush shape; but the fast fracture surface appears to not have this type of phenomenon. These fracture surfaces further show that fatigue fractures can occur at the thin weak points of fibers and fast fracture is carried out between the fibers using the coordinated method. The surface differences of fatigue

fractures and fast fractures can be used to analyze the fatigue damage of the composite parts.

Figures 7a, b and c are the fracture surfaces formed under different fatigue loads (i.e. different $\triangle K$). By comparing them, we can know that their fatigue sectional morphology is related to the fatigue load level. When compared with a high load, the low load causes relatively rough fatigue fracture surfaces. Therefore, after the part or sample fractures, we can also perhaps compare the surface morphologies to determine the sequence of the size of each location's fatigue stress.

Conclusion

Based on the above test results and observations, we can make the following conclusions:

1. Fatigue crack propagation results show that the fatigue crack process is controlled by the cyclic stress intensity factor range. When this factor approaches the fracture toughness of the material, the fatigue crack propagation rate generally increases rapidly. The m values of the two types of materials used in this paper are both higher than that of common metal. The crack propagation ra te of woven composites is also higher than that of non-woven fiber composition.

2. Observations of the interior ply of the samples showed that fiber fractures caused weak points to occur in the front part of the fracture and the fibers were clearly produced at the interwoven point.

3. The fracture surface morphology shows that the fatigue crack surface is rougher than the fast fracture surface and the fiber pull-out is noticeable.

References

[1] Wu, E.M., Fracture Mechanics of Anisotropic Plate in Tsai, S.W. et al, Eds., Composite Materials Workshop, Technomic Publishing Company, Stamford, Conn. 1968, 20-43.

[2] Phillip, D.C., J. Compos. Mater., 8(4), (1974), 130-140.

[3] Mandell, F.J., Mcgarry, F.J., Wang, S.S. and J.Im., same as above, 106-116.

[4] Sun, C.T. and Chan, W.S., in Composite Materials, Testing and Design (Fifth Conference), ASTM STP 674, 1979, 418-430.

[5] Hertzberg, R.W., Deformation and Fracture Mechanics of Engineering Materials, Wiley, New York, 1976.

[6] Tada, H., Paris, P.C. and Irwin, G.R., The Stress Analysis of Cracks Handbook, DEL Research Corpora tion, Hellertown, Pennsylvania, 1973.
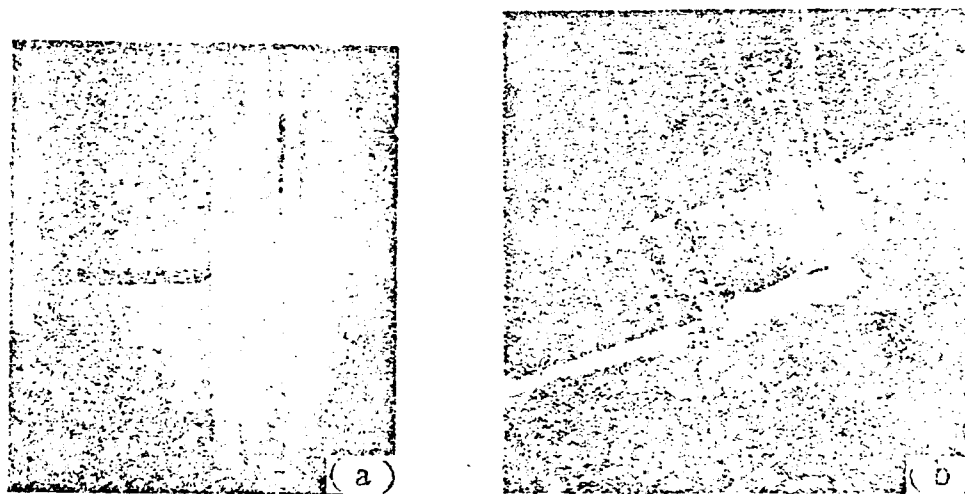
Fig. 4 Debonded tearing lamination and bell shaped stripping of [0/90]$_{5s}$ non-woven composite sample.
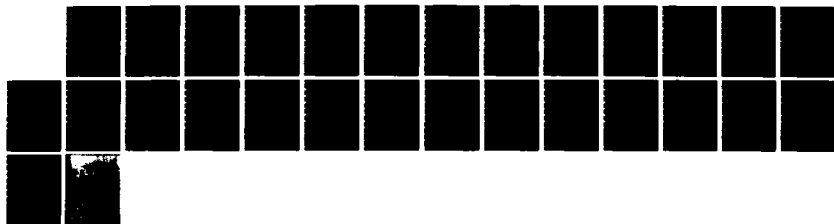
Key: (a) Before final fracturing; (b) After fracturing.
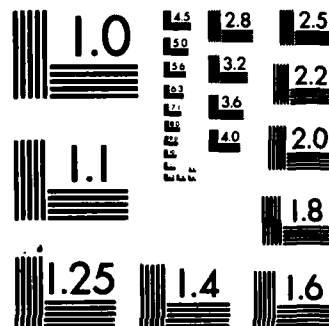
MICROCOPY RESOLUTION TEST CHART
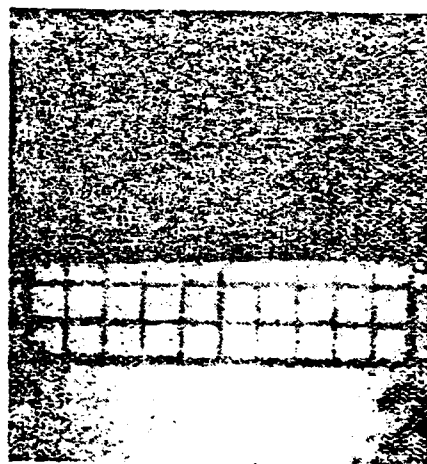
NATIONAL BUREAU OF STANDARDS-1963-A

Fig. 5   Photo of internal ply of $[0/90]_{5s}$ sample.

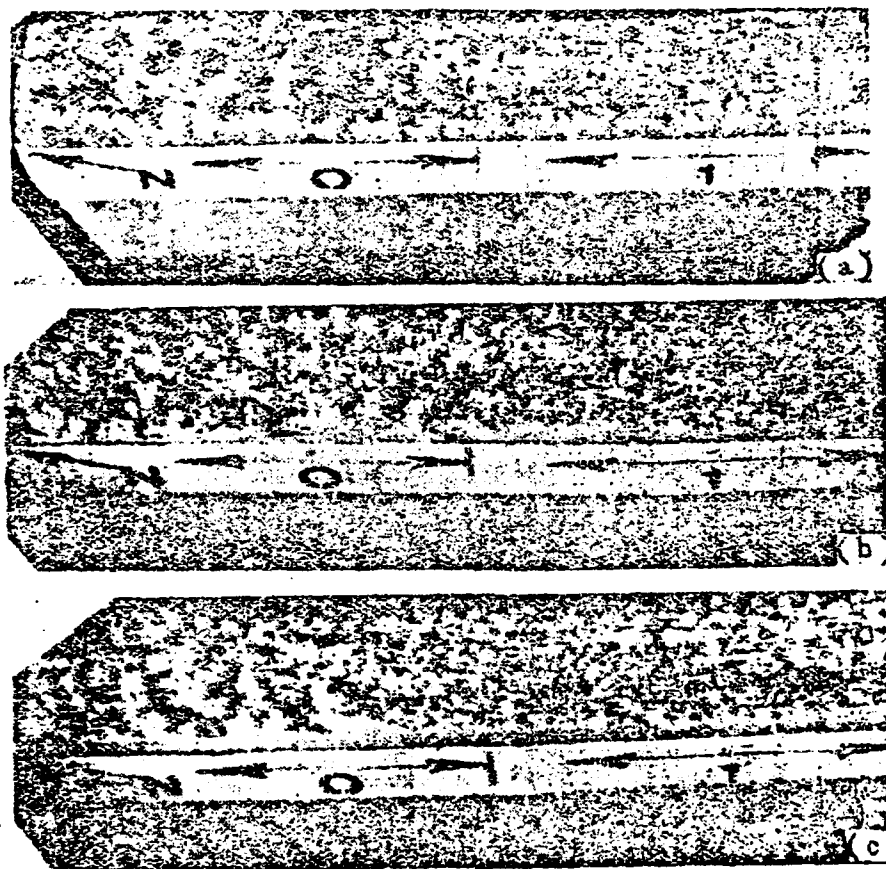Fig. 6   Photo of internal ply of woven sample.

93

Fig. 7 Fracture surface morphology of woven sample.

Key: (a) F-B-0.2, P_{max}=113kg; (b) F-B-13, P_{max}=145kg;
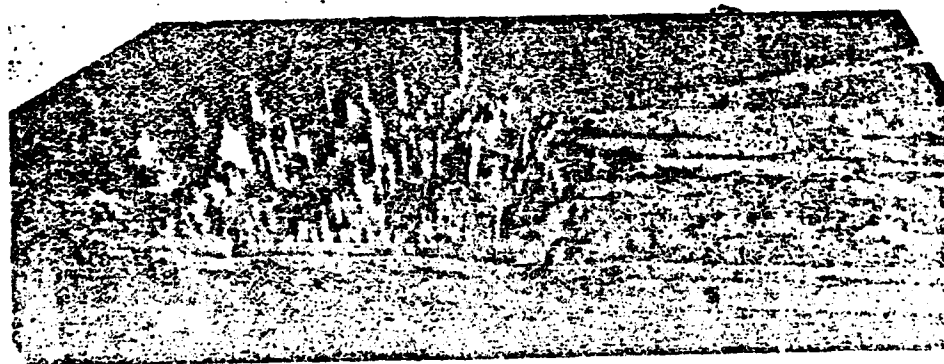(c) F-B-11, P_{max}=159kg.

Fig. 8 Fracture surface morphology of non-woven fiber composite sample.

STUDY OF THE THERMAL MECHANICAL FATIGUE PROPERTIES OF GH33A ALLOY

Wang Haiqing

Abstract

We studied the thermal mechanical fatigue (TMF) and low cycle fatigue (LCF) properties of the high temperature alloy GH33A under 330 $\leftrightharpoons$ 700°C and 700°C.

Therman mechanical fatigue test results showed the relationship between elastic strain range $\Delta\varepsilon_p$ and half stress range $\Delta\sigma/2$, and the lifetime can be expressed by the Coffin-Manson law:

$$\Delta\varepsilon_p = 0.054 M_f^{-0.054}$$
$$\Delta\sigma/2 = 1.97 N_f^{-0.074}$$

Fatigue hardening occurs during the early stage. The relationship between half stress range $\Delta\sigma/2$ and the half elastic strain range is as follows:

$$\Delta\sigma/2 = 1.9(\Delta\varepsilon_p/2)^{0.14}$$

The temperature cycles decrease the life and promote fracturing along the crystal.

These test results can act as a basis for engine part selection of materials and design.

Preface

GH33A alloy is used to make the first and second level turbine disk material for the WP-7 engine. The service temperature is 700°C. On the basis of the GH33 alloy, the GH33A alloy slightly raised the Al and Ti contents and added in the nickel base

95

austenite effective alloy with 1.3-1.6% Nb.

At present, the problem which urgently awaits resolution is fixing the life of the WP-7 engine. However, the turbine disks are the heart of the engine and are the key components which limit the life of the engine. After design units carried out finite element analysis it was shown that because of the superposition of the centrifugal force and thermal stress, in the 350-700°C temperature range, the local area of this turbine disk has already had plastic deformation. Therefore, it is doubtful that thermal mechanical fatigue tests of GH33A alloy are even closer to the situation of these disks than high temperature low cycle fatigue tests to provide valuable data for determining the life of these disks.

Material and Test Method

The chemical composition of GH33A alloy is (%): $c \leqslant 0.07$; Cr, 19-22; Ni, the remainder; Al, 0.7-1.2; Ti, 2.5-3.0; Nb, 1.3-1.6; Si $\leqslant 0.65$; Mn $\leqslant 0.35$; B $\leqslant 0.01$; Ce $\leqslant 0.01$. See Table 1 for its conventional mechanical properties. The thermal process system is: maintain a temperature of 1080°C for 8 hours, air cool; maintain a temperature of 750°C for 16 hours, air cool.

(1)温 度 °C	(2) 温变及湿 σb, kg/mm²	(3) 屈服强度 $\sigma 0.2$, kg/mm²	(4) 伸长率 δ, %	(5) 面缩率 ψ, %	(6) 弹性模量 $E \times 10^3$, kg/mm²
20	122.1	77.7	17.9	25.7	22.76
700	199.8	63.8	20.9	21.6	18.64

Table 1   Conventional mechanical properties of GH33A alloy.

Key: (1) Temperature; (2) Intensity limit; (3) Yield strength; (4) Elongation; (5) Contraction; (6) Elastic modulus.

96

See Reference [1] for the shape, dimensions of the sample and the test method.

The tests were carried out on a 10 ton electrolytic servo thermal fatigue tester. The test conditions were as follows:

1. 700°C Low Cycle Fatigue Test (LCF)

Control strain, triangular waves (see Fig. 1); the test frequency was determined by the $f = \varepsilon_\gamma / (2\Delta\varepsilon_T)$ formula ($\Delta\varepsilon_T = 0.002/\text{seconds}$); strain ratio $R\varepsilon = -1$.

2. 330 $\leftrightharpoons$ 700°C Thermal Mechanical Fatigue Test (TMF).

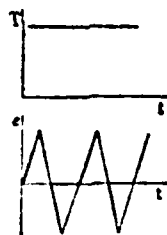Control load, trapezoidal waves (see Fig. 2); test frequency $f = 0.004\text{Hz}$; stress ratio $R\sigma = -1$.

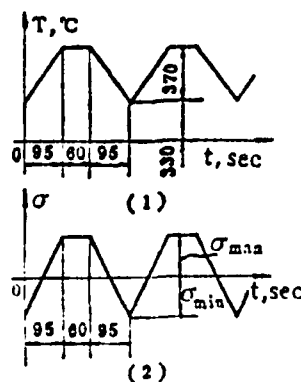
Fig. 1 LCF temperature and strain waveform.

Fig. 2 TMF temperature and strain waveform.

97

Test Results

1. The test results of the fracture life are the stress and strain range measured when using $N_f/2$ and based on the $\sigma = E\varepsilon$ formula we indicated the elastic strain range $\Delta\varepsilon_e$ and then used the $\Delta\varepsilon_p = \Delta\varepsilon_T - \Delta\varepsilon_e$ formula to obtain plastic strain range $\Delta\varepsilon_p$. They are separately drawn into $\Delta\varepsilon_T$, $\Delta\varepsilon_e$ and $\Delta\varepsilon_p$ and double logarithm relational curve of N_f as shown in Figs. 3 and 4.
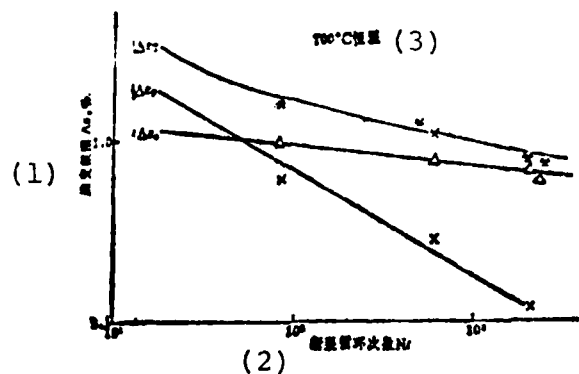

Fig. 3 GH33A 700°C LCF $\Delta\varepsilon$ -N_f curve.
Key: (1) Strain range; (2) Fracture cycle number; (3) Constant temperature.
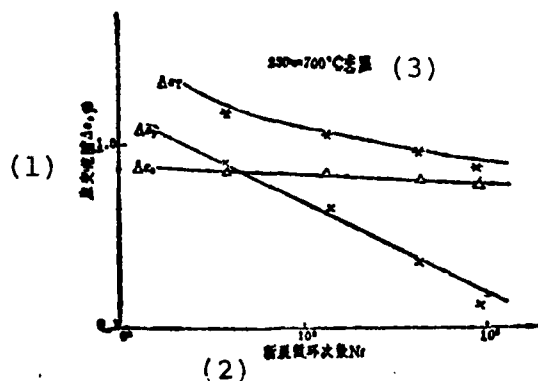

Fig. 4 GH33A 330 $\leftrightarrows$ 700°C TMF $\Delta\varepsilon$ -N_f curve.
Key: (1) Strain range; (2) Fracture cycle number ; (3) Constant temperature.

Based on the Manson empirical formula [2]: $\Delta\varepsilon_p = MN_f^z$ and

98

$\Delta\varepsilon_e = G/EN_f^r$, linear regression is used to fit the linear equation and the values of M, G/E and r in it are listed in Table 2.

(1) 温 度 状 态	M	z	G/E	r
(2) 恒温700°C	0.1192	−0.6272	0.0163	−0.1362
(3) 变温330⇌700°C	0.0540	−0.5391	0.0092	−0.0735

Table 2 Test values of constants M, z, G/E and r.
   Key: (1) Temperature state; (2) Constant temperature;
   (3) Variable temperature.

2. The $\Delta\sigma$ -N_f curve measured in the life test process is as shown in Fig. 5.
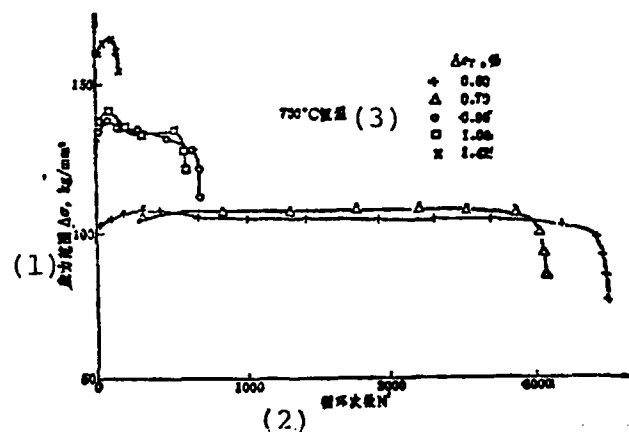

Fig. 5 GH33A 700°C LCF $\Delta\sigma$ -N curve.
   Key: (1) Stress range; (2) Cycle number; (3) Constant temperature.

3. A comparison of GH33A 700°C LCF and 330⇌700°C TMF lifetimes is shown in Fig. 6.
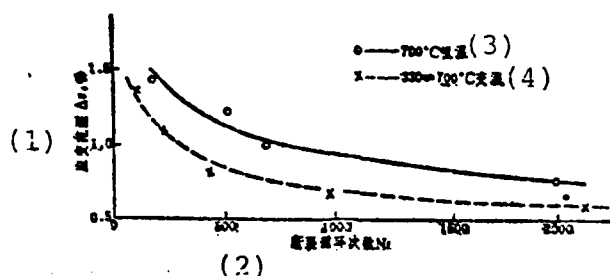
Fig. 6 Comparative curves of GH33A 700°C LCF and 330 ⇆ 700°C
TMF lifetimes.

Key: (1) Strain range; (2) Fracture cycle number;
(3) Constant temperature; (4) Variable temperature.

4. The $\Delta\sigma/2$-Nf curve of GH33A 700°C LCF and 330 ⇆ 700°C
TMF is shown in Fig. 7. The Manson-Coffin equations are

$$\Delta\sigma/2 = 2.18 N_f^{-0.14} \quad (700°C \ LCF)$$
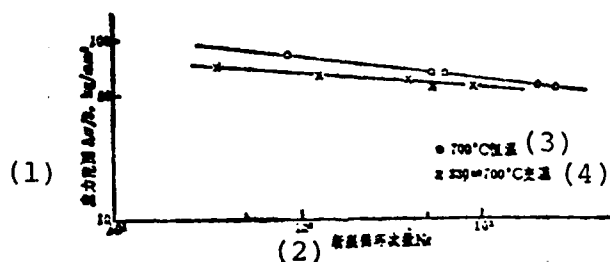$$\Delta\sigma/2 = 1.97 N_f^{-0.074} \quad (330 \rightleftharpoons 700°C \ TMF)$$

Fig. 7 The $\Delta\sigma/2$-Nf curve of GH33A 700°C LCF and 330 ⇆ 700°C
TMF.

Key: (1) Stress range; (2) Fracture cycle number;
(3) Constant temperature; (4) Variable temperature.

5. The $\Delta\sigma/2$-$\Delta\varepsilon$ p/2 curve of GH33A 700°C LCF and
330 ⇆ 700°C TMF is shown in Fig. 8. The stress-strain relational
formulas are

100

$$\Delta\sigma/2 = 1.98\left(\Delta\varepsilon_e/2\right)^{0.18} \quad (700\ C\ LCF)$$

$$\Delta\sigma/2 = 1.90\left(\Delta\varepsilon_p/2\right)^{0.14} \quad (330 \rightleftharpoons 700\ C\ TMF)$$
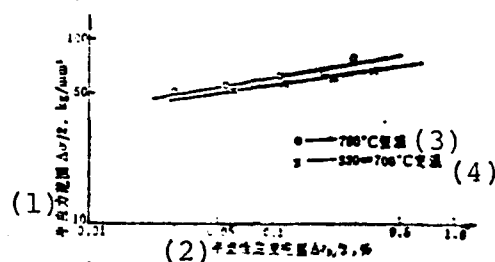
Fig. 8 The $\Delta\sigma/2 - \Delta\varepsilon_p/2$ curve of GH33A 700°C LCF and 330 $\rightleftharpoons$ 700°C TMF.

Key: (1) Half stress range; (2) Half elastic strain range; (3) Constant temperature; (4) Variable temperature.

6. Metallographic Analysis Results

The results of using a scanning electron microscope to analyze the fatigue fractures are shown in Figs. 9 and 10 (see Plate 14). The results show that 700°C low cycle fatigue fractures are the transcrystalline type and the fatigue strips are clear; but the 330 $\rightleftharpoons$ 700°C thermal mechanical fatigue fractures are along the crystal type.

Discussion

1. Thermal Mechanical Fatigue Properties of GH33A Alloy

By comparing the life curves of the high temperature low cycle fatigue and thermal mechanical fatigue of GH33A alloy, we can conclude that the thermal mechanical fatigue life is relatively low (see Fig. 6). The reasons for the life being low will be

discussed later. Here, we will only explain that use of the thermal mechanical fatigue to calculate the service life of the turbine disk is even closer to the real conditions than using low cycle fatigue and it tends to be safer.

The transit $\cdot$ n life N_t of the GH33A alloy (see Figs. 4 and 5 wherein the life $\cdot$rresponding to the intersecting point of the two straight lines $\Delta\varepsilon$ e and $\Delta\varepsilon$ p is called transition life N_t) is relatively low which shows that it is not beneficial for the designed life N_D to be smaller than N_t. It should be designed in a state larger than N_t which will bring into play the strength potential of this alloy. That is, it is advantageous to select the total strain range between 0.4-0.6%.

We can use plastic strain range $\Delta\varepsilon_p$ to calculate the thermal mechanical fatigue life of GH33A alloy. Its expression is as follows:

$$\Delta\varepsilon_p = 0.054 N_f^{-0.5391}$$

2. Reasons Causing the Decreases of the Thermal Mechanical Fatigue Life

Thermal mechanical fatigue is a type of compound fatigue, that is, the superposition of the thermal strain, mechanical strain and creep strain. The reasons for decreases in the life are also multifaceted. This paper carries out preliminary discussion focusing on the following three points:

(1) The temperature circulation speed of this test is relatively slow (T=41 minutes). There is also certain retention time of the upper limit temperature (t_H=1 minute) and thus the creeping damage effects of the material increase, the cracks along the crystal tend to intensify and under the interaction of fatigue and creeping it accelerates the fatigue fracturing process.

102

(2)   The superposition of microscopic thermal stress.   In local areas, carbides, inclusions etc. exist in the alloy. They have discrepencies with the base body's thermal expansion coefficient, heat conduction coefficient and elastic module and during the heat circulation process, it is not possible for these particles to have the same expansion and contradiction deformation as the base body.   Thus, microscopic thermal stress is necessarily created in the vicinity of the intersection surface of the two.   D. Margrave [3] used a film electron microscope to observe the plastic deformation caused by the microscopic thermal stress produced around the carbide in the material after temperature circulation.   Under the effects of heat circulation, this area is the source of the microcracks.   Moreover, it can also accelerate the propagation of the main cracks.

(3)   Influences of the crystal boundary state.   Coffin [4] considers that local intercrystalline oxidation has important effects in the crack nucleation and propagation processes.   The oxidation can diffuse along the crystal boundary and when there is high temperature circulation strain, the strain is concentrated on the crystal boundary and the crystal boundary's relative slide causes the embrittled oxidant to crack.   When observing with a film transmission electron microscope, we discovered that the Cr diluted zone of the crystal boundary with heat circulation widened (Figs. 11 and 12, see Plate 14) causing the oxidation resistance of the crystal boundary to decrease and the oxidation diffusion of the crystal boundary to accelerate.

Conclusion

1.   Under the conditions of this test, the thermal mechanical fatigue life of the GH33A alloy was lower than the high temperature low cycle fatigue life.

2.   When using this alloy, designed life N_D should be larger

than transition life N_t. We can use the following formula to calculate the thermal mechanical fatigue life:

$$\Delta \varepsilon_p = 0.05 dN_f^{-0.5391}$$

3. GH33A alloy produces circulation hardening at 700°C.

4. Under constant stress, the calculation formula for the life of GH33A 330 ⇋ 700°C TMF is:

$$\Delta \sigma / 2 = 1.97 N_f^{-0.074}$$

5. For the n'=0.14 of GH33A 330 ⇋ 700°C TMF, the relationship of the half stress range and half elastic range is:

$$\Delta \sigma / 2 = 1.90 \, (\Delta \varepsilon_p / 2)^{0.14}$$

6. 700°C low cycle fatigue is transcrystalline fracturing and 330 ⇋ 700°C thermal mechanical fatigue is fracturing along the crystal.

7. Improvement of the GH33A alloy should focus on strengthening the crystal boundary and raising its ability to resist plastic deformation.

Ge Songsheng, Yang Fu, Guo Xiufen and Han Zengxiang as well as graduating students Wang Hong and Wu Rui of Department 102 of the Aeronautics College of Beijing also participated in this work.

References

[1] Wang Haiqing et al, Summary of Low Cycle Thermal Fatigue test Methods and Techniques (Internal Materials), Beijing Institute of Aeronautical Materials, 1980.

References (continued)

[2]   Manson, S.S., Thermal Stress and Low-cycle Fatigue, 1974.

[3]   Margrave, D., J. of the Iron and Steel Institute, 203, (1956), 386-391.

[4]   Coffin, L.F., ASTM STP520, (1973).

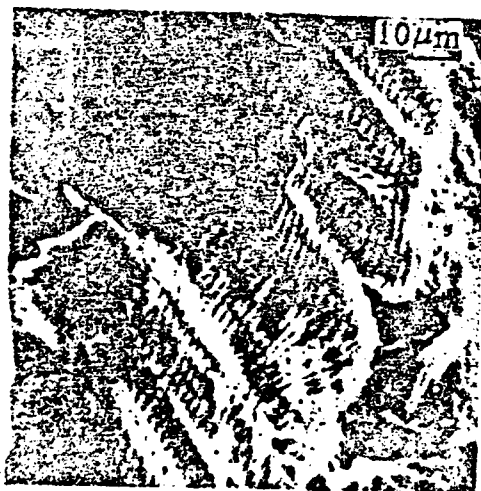Fig. 9   700°C   LCF fracturing (transcrystalline, fatigue strips).

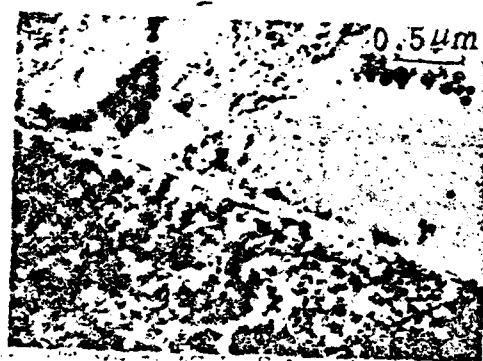Fig. 10   300 ⇆ 700°C   TMF fracturing (along the crystal, brittle fracturing.

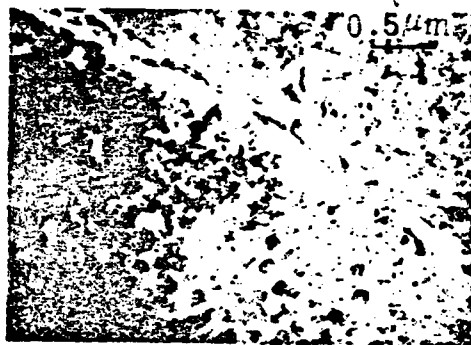Fig. 11   700°C   LCF sample, $\Delta \varepsilon_T = 0.61\%$.

Fig. 12 330 ⇆ 700°C TMF sample, $\Delta\varepsilon_T$=0.67%.

APPROXIMATE CALCULATION OF THE NOTCH STRENGTH OF METALLIC MATERIALS

Zheng Xiulin

Northwestern Polytechnical University

The paper proposed models of the crack initiation at the notch root and the fracture of notched elements under low stress brittle fracture conditions. Based on this, we derive the approximate calculation formulas for the notch strength of various metallic materials and examine the test results in suitable references. Finally, we attempt to propose a new material constant, the insensitive-to-notch factor whose value can be estimated from the tensile properties.

Preface

At the beginning of the 1960's, a great deal of experimental research was conducted on the notch strengths of various types of metallic materials such as high strength steel, aluminum alloys and titanium alloys etc. [1-3]. A good part of this research has been compiled into metallic structural materials handbooks in the United States [4,5] and they make up the significant contents of the manuals. Recently, some people have emphasized using the ratio of the notch strength to the yield strength as the reference standard of product quality control [6]. Although Sachs et al gave the empirical formulas of the brittle metal's notch strength [1], to date, there is still no formula which can be used to estimate the notch strength of plastic metallic materials. Moreover, we have still not seen theoretical analysis of this problem in the references.

Based on the advances in research on the notch's stress-strain analysis as well as line elastic fracture mechanics [7,8], this paper proposes models of the crack initiation at notch root and the fracture of notched elements under low stress brittle

108

fracture conditions and based on this we derive the formulas for the notch strengths of various metallic materials. Finally, we propose the use of a new material constant, the so-called insensitive-to-notch factor and give the corresponding calculation formulas.

Theoretical Analysis

The fracturing of notched elements or samples possibly includes three stages: the crack initiation at notch root, subcritical propagation which possibly occurs at the cracks beginning at the notch root and the final fracturing. After the cracks begin at the notch root, its total length is adding a small section of the initial crack length on the notch depth. If the crack length reaches the critical value after the cracks begin at the notch root, then the notched element or sample will fracture when the cracks do not have subcritical propagation. Under these circumstances, the crack primary stress at the notch root, which is approximately equal to the fracture stress, is the notch strength.

We can hypothesize that the crack initiation at the notch root is caused by the fracturing of the material element at the notch root as shown in Fig. 1. Similar models were proposed in fatigue research [9,10].
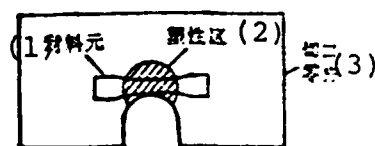

Fig. 1 Schematic of the single axis material element of the notch root concept.

Key: (1) Material element; (2) Plastic area; (3) Notched element.

The crack initiation at the notch root, which is to say, the fracturing of the notch root's material element, is determined by the local stress (σ) or local strain (ε) of the notch root as well as the properties of the material. Based on the deformation and fracture characteristics during tensile tests, the metallic materials can be divided into three categories: the brittle metals, low plastic metals and high plastic metals. Brittle metals do not have plastic deformation when there is tension and therefore its elongation (δ %) and sectional contraction (ψ %) are both zero, that is, δ %=ψ %=0; moreover its tensile strength (σ_b) is equal to its fracturing strength (σ_f) and equal to and even lower than its yield strength (σ_s). Low plastic metals only have uniform elongation but do not have necking when there is tension and therefore its sectional contraction is larger than its elongation.

Different types of materials follow different fracturing norms. The brittle materials follow the positive stress fracturing norm. When the notched sample or element sustains tensile load, due to the stress concentration, the local stress of the notch root is equal to the sum of the theoretical stress concentration coefficient (K_t) and defined stress (S), that is, $\sigma = K_t S$. When the local stress reaches the value of the fracture strength, that is

$$K_t S = \sigma_f \qquad (1)$$

then the material element of the notch root has fracturing and forms cracks as shown in Fig. 1. Based on the above mentioned model and formula (1), we can obtain notch strength σ_N of the brittle metallic material:

$$\sigma_N = \sigma_f / K_t \qquad (2)$$

The high plastic metallic material follows the positive strain fracturing norm. Although the defined stress sustained by the notched element is lower than the yield strength under the absolute majority of engineering applications, yet because of the

110

stress concentra tion, the local stress of the notch root can
exceed the yield str ength and form a plastic area at the notch
root. When the plastic strain of the notch root's material
element reaches the value of the metal's fracturing ductility
($\mathcal{E}_f$), then the material element of the notch root has fractur-
ing and forms cracks. Based on this hypothesis, Reference [7]
gives the crack initiation norm at the notch root of high
plastic metals as follows:

$$K_{ts} = \sqrt{E \sigma_f \varepsilon_f} \qquad (3)$$

In the formula, E is the Young's modulus. Fracturing strength
(σ_f) and fracturing ductility ($\mathcal{E}_f$) can be calculated by the
following formulas [7]:

$$\sigma_f = \sigma_b (1 + \psi) \qquad (4a)$$

$$\varepsilon_f = -\ln (1 - \psi) \qquad (4b)$$

Nevertheless, Reference [7] is unable to give further theor-
etical discussion and test proof of formula (3). Statistical
analysis of the test data [4,5] shows that most of the
$\sqrt{E \sigma_f \varepsilon_f}$ value of the metallic structural material is between
0.05-0.15E. More stringent analysis shows that, in engineering
terms, the theoretically integrated strength of the material
can be called the theoretical fracturing strength and its value
is 0.05-0.1E [11]. Therefore, the value of $\sqrt{E \sigma_f \varepsilon_f}$ can be
considered as a type of measurement of the theoretical fracture
strength of industrial metals. Therefore, the mechanical mean-
ing of formula (3) is: when the value of the notch root's
fabricated elastic stress ($K_t S$) reaches the theoretical fracture
strength, then cracks form at the notch root. Orowan conceived
that at the crack tip the material possibly reaches the theor-
etical strength value [11]. Therefore, we can consider that
formula (3) is the same as Orowan's conception and we can also
consider that it is its elongation. Although we do not have
direct tests on the crack initiation at the crack root, yet the

111

test results in Reference [12] on fatigue crack initial life (N_i) which based on the related formula given in Reference [7] extrapolated $N_i = 1$ cycle can provide indirect proof of formula (3). Because of this, formula (3) can be used to analyze the fracturing of notched elements.

Based on the above fracture models of notched elements and formula (3), we can obtain the high plastic metallic material's notch strength as:

$$\sigma_N = \sqrt{E \sigma_i \varepsilon_f} / K_t \tag{5}$$

Test Results and Discussion

Although we obtained a great deal of valuable data from the experimental research on notch strength, yet only a small portion of this research can be used to make further theoretical investigations. The test results of Sachs et al are highly significant [1] and are shown in Fig. 2.
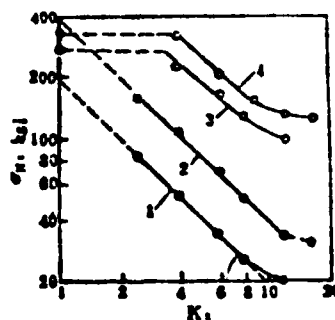

Fig. 2   Test results of the notch strengths of various metals [1].

Key: (1) Brittle metal (Ti-2.5Al-16V alloy undergoes 1400°F for 20 minutes, water quenching, 700°F annealing for 4 hours); (2) 300M steel, -320°F test; (3) Ti-4Al-3Mo-N, -320°F test; (4) 300M steel, room temperature test.

We can see from Fig. 2 that in a certain range the notch

112

strength of the test alloys and the product of the stress concentration coefficient are one constant, that is

$$\sigma_N \cdot K_t = C_N \qquad (6)$$

This result is in complete agreement with the theoretical analysis of the previous section yet formulas (2) and (5) show that the values of constant C_N are different for different types of metals.

The value of C_N for brittle metals should be equal to the fracture strength as shown in formula (2). Sachs et al gave the value of brittle metal C_N as the tensile strength [1]. As pointed out in the previous section, the tensile strength of the brittle metal is the same as the fracture strength value. Therefore, the test results of Sachs et al totally agree with formula (2).

As regards high plastic metals, from formula (5), the value of its C_N should be equal to $\sqrt{E \sigma_f \varepsilon_f}$. It is regrettable that Sachs et al did not give the tensile properties of the high plastic metals and the values of C_N. However, Reference [2] gives the test results of the tensile properties and notch strengths of aluminum and titanium alloys and elastic module E is estimated based on the data given in Reference [4]. In this way, based on formulas (4) and (5), we can estimate the notch strength values of the above mentioned alloys. Tables 1 and 2 list the estimated values and test results of the notch strengths of the above mentioned alloys; aside from the separately listed ones, the absolute majority of the estimated values of notch strengths are close to or lower than the test results. This is because for the cracks which begin at the notch root, there can be various degrees of subcritical propagation before the final fracturing of the notch sample. We have not yet considered this for notched elements or the fracture models of samples. Therefore, we can consider that it is the lower limit of the test measured value based on the notch strength es timated from formula (5).

113

(1) 合 金	试验量要 (2) ·F	σ_b ksi	$\sigma_{0.1}$ ksi	ψ %	σ_t ksi	E ksi	ε_t	σ_N, ksi (7 计算值)	测定值 (8)
Ti—7Al—4Mo (3) 室 温		160	154	38.0	220.8	18200	0.478	124.9	143
	−105	188	180	31.0	246.3	18300	0.371	116.5	151
	−240	208	197	32.0	274.6	18340	0.386	125.6	148
	−320	241	224	26.0	303.7	18540	0.301	117.3	139
Ti—7Al—3Mo (4) 室 温		161	155	30.0	209.3	18200	0.357	105.0	153
	−105	186	181	24.0	230.6	18300	0.274	97.0	146
	−240	214	203	25.0	267.5	18340	0.289	107.0	139
	−320	240	219	25.0	300.0	18540	0.289	114.2	138
Ti—6Al—4V (5) 室 温		143	133	52.0	217.4	16400	0.734	145.7	152
	−105	171	162	43.0	241.5	17400	0.562	139.3	165
	−240	198	189	45.0	287.1	18170	0.589	159.1	177
	−320	221	214	43.0	316.0	18630	0.562	163.9	173
Ti—16V—2.5Al (6) 室 温		129	88	23	158.7	16400	0.260	74.3	124
	−105	182	151	20	218.4	17400	0.223	83.0	126

Table 1   Tensile properties and notch strengths of titanium alloys, K_t=11.1 [2,4].

Key: (1) Alloy; (2) Test temperature; (3)-(6) Room temperature; (7) Calculated value; (8) Measured value.

(2)

(1) 合金	试验温度 °F	σ_b ksi	σ_{0.1} ksi	ψ %	σ_f ksi	E ksi	ε_f	σ_N, ksi 计算值 (3)	σ_N, ksi 测定值 (4)
7075—T6	75	82	69	34.7	110.5	10600	0.426	63.6	71.0
	−105	86	73	26.0	108.4	11310	0.301	54.7	61.0
	−240	92	78	24.0	114.0	11860	0.274	54.9	66.0
	−320	98	81	23.4	120.9	12180	0.267	56.5	64.0
2024—T3	75	72	50	32.4	95.3	10600	0.392	56.7	60.0
	−105	74	52	24.3	92.0	11310	0.278	48.5	62.0
	−240	78	55	22.6	5.6	11860	0.256	48.5	67.0
	−320	87	64	16.5	101.4	12180	0.180	42.5	73.0
Alclad 2024—T3	75							56.7	55.0
	−105							48.5	59.0
	−240							48.5	64.0
	−320							42.5	67.0
6061—T6	−240	59	49	45.5	85.8	11860	0.607	70.8	53.0
	−320	64	52	41.6	90.6	12180	0.538	69.4	57.0
2014—T6	75	76	65	38.0	104.9	10780	0.478	66.2	68.0
	−320	85	72	26.0	107.1	11860	0.301	55.7	73.0

Table 2 Tensile properties and notch strengths of aluminum
alloys, K_t=11.1 [2,4].
Key: (1) Alloy; (2) Test temperature; (3) Calculated
temperature; (4) Measured temperature.

Based on the tensile property data in Reference [4], at
−320°F, 300M steel should be a low plastic metal; based on form-
ula (4), we estimated its fracture strength value to be about
380ksi (2610MPa) which is close to the test measured value of C_N
(see Fig. 2). Therefore, we consider that we should calculate
the notch strengths of low plastic metals based on formula (2).

The relationship of the notch strength and stress concentra-
tion coefficient shown in Fig. 2 can be called the notch strength
chart. The notch strength chart of a typical brittle metal is
made up of two straight line sections AB and BC as shown in Fig.
3a. In the AB section, the notch strength decreases with the
rising of the stress concentration coefficient. The

115

relationship between them is indicated by formula (2). In the
BC section, the notch strength is a constant (σ_c). Its value
is determined by the notch depth and fracture toughness of the
material and it decreases with the enlargement of the notch
depth. Therefore, the B point will shift to the right and down
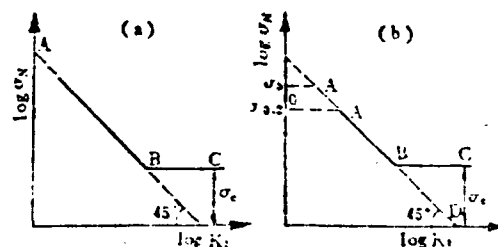along the BD line.

Fig. 3 Typical notch strength chart.
       Key: (a) Brittle metal; (b) High plastic metal.

The notch strength charts of high plastic materials are gen-
erally made up of thr-e stright line sections, that is, OA, AB
and BC, as shown in Fig. 3b. The significance of the AB and BC
sections are as mentioned above; however, in the AB section, the
relationship of the notch strength and stress concentration
coefficient should accord with formula (5). In the OA area, the
primary stress of the notch root's cracks calculated from formula
(3) is equal to or higher than the yield strength and thus the
notch strength is also equal to or higher than the yield strength.
Letting $\sigma_N = \sigma_s$, we obtain the width of the OA area from formula
(5)

$$K_{tn} = \sqrt{E\,\sigma_f\,\varepsilon_f}\,/\sigma_s \qquad (7)$$

Naturally, K_{tn} is the material constant; its mechanical signific-
ance is that when the stress concentration coefficient is equal
to or higher than K_{tn}, the notched element of high plastic metal
does not have low stress brittle fracturing. Therefore, we can

116

call K_{tn} the insensitive-to-notch factor.

In engineering applications, we often use the ratio σ_N/σ_b of the notch strength to the tensile strength as the data of whether or not the metal is sensitive to the notch; when $\sigma_N/\sigma_b \geqslant 1.0$, it is insensitive to notches and when the contrary then it is sensitive to notches. Based on the data in Tables 1 and 2, if the effective application range of formula (5) can be extended to $S \leqslant \sigma_b$, then the AB area can extend out to the A' point along the extended line of BA as shown in Fig. 3b. Letting $\sigma_N = \sigma_b$, we can find width K_N of the O'A' area from formula (5)

$$K_N = \sqrt{E \sigma_f \varepsilon_f}/\sigma_b \qquad (8)$$

Naturally, K_N is also the material constant; its mechanical significance is when $K_t = K_N$, $\sigma_N/\sigma_b \geqslant 1.0$, that is, the material is not sensitive to the notch. Therefore, K_N is also called the insensitive-to-notch factor which is defined based on engineering conventions.

As regards the insensitive-to-notch factor for low plastic materials, K_{tn} and K_N can be calculated from formula (2) as follows:

$$K_{tn} = \sigma_f/\sigma_{0.2}, \quad K_N = \sigma_f/\sigma_b$$

The elongation and sectional contraction of this type of material generally do not exceed 10% but yield strength ratio $\sigma_{0.2}/\sigma_b \approx 0.7-0.8$. Therefore, $K_N \leqslant 1.1$, $K_{tn} \leqslant 1.5-1.6$.

As pointed out previously, for brittle material $\sigma_f = \sigma_b \leqslant \sigma_s$ and therefore $K_{tn} = K_N = 1$. Therefore, we can say that brittle materials are absolutely sensitive to notches.

However, we should explain that when the stress concentration coefficients are the same, the danger of shallow pointed notches having low stress embrittlement and fracturing is relatively small

and the notch sensitivity is also relatively small because the cracks formed in the shallow notch root can have relatively large degree subcritical propagation before fracturing. Therefore, when discussing the notch sensitivity of materials, we must consider the geometrical shape of the element. Nevertheless, K_{tn} and K_N can act as data for determing the sensitivity of materials to notches; we should do further experimental research on this.

Conclusion

1. Metallic materials can be divided into three types based on the deformation and fracturing characteristics when it has tension: brittle material, low plastic material and high plastic material.

2. The models proposed in this paper for the crack initiation at the notch root and the fracture of the notched elements were used to explain the fracturing process of the notched element.

3. This paper derived calculation formulas for the notch strengths of the three above mentioned types of material. However, the formulas did not consider the subcritical propagation of the cracks and therefore calculation of the notch strengths of high plastic metals based on the formulas will under certain circumstances be the lower limit of the test results.

4. This paper proposed the use of a new material constant - the insensitive-to-notch factor. Its value can be estimated based on the tensile properties.

References

[1] Sachs, G. and Sessler, J.G., ASTM STP287, 1960, PP.122-135.

[2] Hickey, C.F.Jr., Proc.ASTM, 62(1962), PP.765-777.

[3] Espey, G.B. et al, ASTM STP287, 1960, PP.74-107.

[4] Aerospace Structural Metals Handbook, Edited by J. Wolf et al, Produced by Mechanical Properties Data Center, Belfour Stulen Inc. 1978.

[5] Structure Alloys Handbook, Produced and Published by Mechanical Properties Data Center, Belfour Stulen Inc. 1979.

[6] Kaufman, J.G. et al, ASTM STP601, 1976, PP.169-190.

[7] Zheng Xiulin, Local Strain Range and Fatigue Crack Initiation Life, to be Published in Proc. IABSE Colloquium, Lausanne, Vol.37, (1982).

[8] Novak, S.R. and Barsom, J.M., ASTM STP601, 1976,PP.409-447.

[9] Standnick, S.T. and Morrow, Jodean, ASTM STP515, 1972, PP.229-252.

[10] Yang Qingxiong, Local Stress-Strain Method of Calculating Fatigue Life, Scientific and Technological Materials of Northwestern Polytechnical University, No. 673.

[11] McClintock, F.A. et al, Mechanical Behavior of Materials, Addison-Wesley Publishing Company, U.S.A., 1966, PP.489-490.

[12] Zheng Xiulin, Mechanical Strength, 1981, No. 3, 1-8.

END

FILMED

6-84

DTIC